Entropy plateaus can emerge from gas replacement at a characteristic halo mass in simulated groups and clusters of galaxies

Altamura, E.; Kay, S.T.; Schaye, J.; McCarthy, I.G.; Schaller, M.

Monthly Notices of the ROYAL ASTRONOMICAL SOCIETY

MNRAS **541,** 3367–3387 (2025) https://doi.org/10.1093/mnras/staf1106
Advance Access publication 2025 July 07

Entropy plateaus can emerge from gas replacement at a characteristic halo mass in simulated groups and clusters of galaxies

Edoardo Altamura [1], Scott T. Kay [1]★, Joop Schaye [2], Ian G. McCarthy [3] and Matthieu Schaller [2,4]

[1] *Jodrell Bank Centre for Astrophysics, Department of Physics and Astronomy, The University of Manchester, Oxford Road, Manchester M13 9PL, UK*
[2] *Leiden Observatory, Leiden University, PO Box 9513, NL-2300 RA Leiden, the Netherlands*
[3] *Astrophysics Research Institute, Liverpool John Moores University, Liverpool L3 5RF, UK*
[4] *Lorentz Institute for Theoretical Physics, Leiden University, PO Box 9506, NL-2300 RA Leiden, the Netherlands*

Accepted 2025 July 3. Received 2025 July 3; in original form 2025 May 8

ABSTRACT

The evolution of the intergalactic medium (IGM) is influenced by gravitational collapse, radiative cooling, and baryonic feedback. Using cosmological hydrodynamic zoom-in simulations of a 8.83×10^{12} $M_\odot$ group and a 2.92×10^{14} $M_\odot$ cluster at $z = 0$, we investigate the emergence of entropy plateaus and their connection to feedback mechanisms. This set-up uses the SWIFT-EAGLE model with three resolutions, down to an initial particle gas mass of 2.29×10^5 and 1.23×10^6 $M_\odot$ for dark matter. We find that, when haloes reach the characteristic mass of $\sim 10^{12}$ $M_\odot$, their entropy profiles flatten at the virial radius, marking a transition from supernova to active galactic nucleus (AGN) feedback-driven regulation. As haloes grow into groups ($\sim 10^{13}$ $M_\odot$), the entropy plateau extends inward and isentropic cores form in massive systems ($\sim 10^{14}$ $M_\odot$). By tracking the Lagrangian history of gas particles, we demonstrate that this entropy buildup is primarily driven by AGN feedback, which efficiently removes low-entropy gas from progenitors of groups and clusters, redistributing it throughout the IGM before falling into the core. Recent observations of X-GAP groups reveal large entropy excesses and plateaus, in line with our findings and in contrast to the power-law-like profiles of most previous observations. While entropy plateaus and large entropy excesses may be observationally confirmed in unbiased samples, reproducing the full diversity of entropy profiles remains an outstanding challenge for next-generation feedback models. Our results suggest that current feedback models may be overly efficient in expelling low-entropy gas from the potential cool-core progenitors, disrupting the balance between heating and cooling required for long-lived cool cores.

Key words: galaxies: clusters: general – galaxies: clusters: intracluster medium – galaxies: evolution – galaxies: formation – galaxies: fundamental parameters – galaxies: groups: general.

1 INTRODUCTION

The evolution of galaxies through cosmic time is deeply intertwined with the complex life cycle of baryonic matter, composed of gas, dust, stars, and black holes (BHs). The baryon cycle describes the gas transfer between the galaxies and their surroundings (intergalactic medium, IGM). It drives the growth of galactic structures and regulates the thermodynamic properties of the IGM. The pathways of the baryon cycle are characterized by interdependent processes, such as star formation, outflows from active galactic nuclei (AGNs), supernova (SN) explosions, radiative cooling, thermal instability, and the gravity-driven accretion of gas back onto galaxies (see Donahue & Voit 2022, for a review).

The transport of gas parcels in an otherwise hydrostatic IGM is governed by buoyancy, whereby cold and dense gas moves towards the centre of the gravitational potential. In contrast, hot and diffuse gas moves away from the centre and stabilizes near gas with similar entropy. In hydrodynamics, this process can be probed with the value of the pseudo-entropy, defined as $K = k_B T / n_e^{(\gamma-1)}$ in terms of the temperature T, the electron number density n_e, and the adiabatic index γ of the ionized gas, with k_B the Boltzmann constant.[1] Low-entropy gas sinks to lower 'altitude', i.e. towards the centre, while high-entropy gas buoyantly rises towards higher altitudes, generating convective motions that tend to align the entropy gradient with the gradient of the gravitational potential (Schwarzschild criterion, see Schwarzschild 1958; Lebovitz 1965; Thorne 1966).

These conditions can be recreated in non-radiative (NR) simulations of groups and clusters and lead to self-similar power-law-like entropy profiles, characterized by low-entropy levels in the core and higher entropy at the virial radius (Tozzi & Norman 2001; Voit, Kay & Bryan 2005). X-ray observations of groups and clusters with masses $10^{13} - 10^{15}$ $M_\odot$ similarly reveal entropy profiles with a median power-law behaviour outside the core (Sun et al. 2009; Pratt et al. 2010).

[1] The pseudo-entropy K, referred to as entropy in this work, is related to the classical thermodynamic entropy as $S \propto \log K$. We direct the reader to Bower (1997) for the derivation of K for a mono-atomic gas, which has $\gamma = 5/3$ and hence $K = k_B T / n_e^{2/3}$.

★ E-mail: scott.kay@manchester.ac.uk

Here, the radial entropy distribution appears to follow a universal power-law profile (Walker et al. 2012) with a logarithmic slope of $\mathrm{d}\log K/\mathrm{d}\log r \equiv \alpha_K \approx 1.21$ (Voit et al. 2005). The fundamental physics underpinning the universality of this feature has not been fully explored. Two explanations attempt to describe the steady-state entropy profile of the IGM gas and the dark matter (Faltenbacher et al. 2007; Hansen & Sparre 2012). The first uses statistical physics to maximize the entropy functional for a self-gravitating particle ensemble in steady state to obtain power-law/polytropic-like profiles (Plastino & Plastino 1993; He & Kang 2010; Beraldo e Silva et al. 2015). The second approach suggests that the power-law index in macroscopic entropy profiles arises from dynamical effects, like radial orbit instability, phase mixing, or violent relaxation that occur during the halo-assembly history (e.g. Kandrup, Vass & Sideris 2003; Henriksen 2009; Diemer 2022).

Notwithstanding the self-similar scaling close to the virial radius, groups and clusters show a remarkably diverse entropy distribution in their cores, where baryonic processes are important (Diemer 2022). In fact, X-ray observations of groups (Sun et al. 2009) and the REXCESS clusters in Pratt et al. (2010) confirmed that significant variation in the entropy profiles is present near the core. Groups and clusters with a small (≈ 3 keV cm^2) excess entropy in the core over a power-law baseline are classified as cool-cores (CC), while large (≈ 75 keV cm^2) entropy excess characterizes non-cool-core (NCC) objects.

According to X-ray observations, the CC population of clusters is measured to be up to 64 per cent of the total – analysing an X-ray-selected sample of clusters, Andrade-Santos et al. (2017) and Rossetti et al. (2017) found that the CC population was 44–64 per cent of the total, depending on the CC definition. However, these samples are affected by the CC bias (Eckert, Molendi & Paltani 2011), which favour concentrated and X-ray-bright CCs (Lin et al. 2015; Rossetti et al. 2017). Instead, the CC bias does not affect Sunyaev–Zeldovich (SZ)-selected samples as they are close to being mass-limited, showing much lower CC fractions observed by Andrade-Santos et al. (2017) and Rossetti et al. (2017) (28–59 per cent) and found to be weakly dependent on redshift (McDonald et al. 2017). On the other hand, hydrodynamic simulations predict different scenarios. In some cases, CC clusters make up the vast majority of the population (e.g. CLuster Evolution and Formation, CLEF, results from Kay et al. 2007, and MAssive ClusterS and Intercluster Structures, MACSIS, simulations from Barnes et al. 2017a), and in other cases, most of the objects have an NCC (e.g. Cluster-EAGLE sample, Barnes et al. 2017b, and the extended sample of Altamura et al. 2023, henceforth Paper I). As an intermediate case, the study of Braspenning et al. (2024) using the FLAMINGO simulations (fiducial model, L2p8_m9, Schaye et al. 2023) predicts a CC fraction similar to TNG-Cluster (Lehle et al. 2024) and marginally higher than ILLUSTRISTNG (Barnes et al. 2018), particularly when using a self-similarly evolving cooling-time criterion to discriminate CC from NCC clusters. Without the time-evolving factor, however, the FLAMINGO CC fraction increases at higher redshifts, in conflict with observations of an approximately constant factorless CC fraction (McDonald et al. 2017; Ruppin et al. 2021). Finally, the low-redshift CC fraction in simulations like MAGNETICUM *Box2b/hr* (Dolag et al. 2015; González Villalba, Dolag & Biffi 2025) and ILLUSTRISTNG (Pillepich et al. 2018) appear to be in reasonable agreement with observations when selecting objects by central electron number density and the scaled concentration parameter, but not when selecting by central entropy (Barnes et al. 2018). Table 1 contains a compilation of studies of simulated groups and clusters quoting their subgrid model, resolution parameters and whether enough CCs are produced to match observations.

Over the past two decades, reproducing the CC fraction in simulations proved to be challenging for two reasons: first, the observed fraction of CC does not emerge *ab initio* from the cosmological parameters used; secondly, the impact of feedback and cooling on group and cluster cores is non-linear and depends on several strongly correlated subgrid parameters (Borgani & Kravtsov 2011), complicating the fine-tuning of the model. So far, no explicit attempt has been made to control the CC fraction in cosmological simulations and theoretical predictions for observations are generally calculated a posteriori with a subgrid model calibrated on galaxy-related quantities (e.g. Crain et al. 2015).

In Paper I, we investigated hot gas and star fractions and entropy profiles at $z = 0$ in groups and clusters, simulated with a version of the SWIFT-EAGLE model similar to that presented in Borrow et al. (2023). This prescription, based on the original EAGLE Ref subgrid of Schaye et al. (2015) and implemented in the SWIFT hydrodynamics simulation code (Schaller et al. 2024), produced too small or absent CCs, defined by the central entropy excess, K_0 (Pratt et al. 2010). Overall, the entropy profiles were flat for all the 27 objects considered at $z = 0$, corresponding to entropy levels in the core ($0.15\,r_{500}$) up to 1 dex too high compared to observations of like-mass objects (Sun et al. 2009; Pratt et al. 2010). On the other hand, recent studies of the X-GAP groups (Eckert et al. 2024) highlighted several entropy profiles that are significantly flatter than previous observations.

Other simulation codes implementing cosmological accretion, feedback and cooling were also found to produce flat or very shallow entropy profiles with small or absent CCs. We have previously shown this effect for EAGLE (Schaye et al. 2015) and Cluster-EAGLE (Barnes et al. 2017b). Other works (see Oppenheimer et al. 2021, and references therein) found similar results for SIMBA (Davé et al. 2019) and FABLE (Henden et al. 2018). The entropy profiles in ILLUSTRISTNG also show a plateau around cluster cores similar to that of Paper I and return a CC fraction much lower than observations when selecting objects by K_0 (Barnes et al. 2018). Breaking the trend, higher resolution models that ignore metal-line cooling above a gas temperature of 10^4 K, like ROMULUS-C (Tremmel et al. 2017), or model isolated halos without cosmological accretion, like Nobels et al. (2022) and Huško et al. (2022), produced a relatively long-lived CC and a power-law-like entropy profile. Moreover, recent work by Huško et al. (2024) suggests that even in idealized objects, entropy profiles can be sensitive to the AGN feedback implementation: thermal isotropic schemes, as in the SWIFT-EAGLE model, tend to produce high entropy in the core, as do kinetic jets without fine-tuned jet particle velocity. However, a combination of the two schemes (hybrid prescription, in their work) can generate stable power-law-like profiles in the 10^{14-15} M$_\odot$ range, while 10^{13} M$_\odot$ groups still produce an entropy plateau in the core.

More recent analyses of the TNG-Cluster sample (Nelson et al. 2024), a re-simulation of 352 cluster regions from the TNG300 volume, showed that the ILLUSTRISTNG model produces CC clusters, being located at one extremum of a unimodal distribution (Lehle et al. 2024) (in contrast with the bimodal K_0 distribution of Pratt et al. 2010), but their abundance depends strongly on the selection criteria, confirming the results of Barnes et al. (2018). Some TNG-Cluster entropy profiles also show an isentropic flat core, similarly to the cluster in Paper I.

The formation of isentropic cores may be the outcome of the entropy-truncation mechanism, proposed by Knight & Ponman (1997), Bryan (2000), Voit & Bryan (2001), and Voit et al. (2002). According to this process, the IGM gas subject to extreme cooling (condensation) or extreme heating no longer contributes to the entropy distribution, which becomes truncated at low values of K and

Table 1. Mass resolution and softening lengths for different types of simulations. The simulations introduced in Paper I are highlighted in orange, and the high-resolution group introduced in this paper is highlighted in yellow. All highlighted runs are used in our analysis. The mass of DM particles is expressed by $m_{\rm DM}$ and the initial mass of gas particles is $m_{\rm gas}$. $\epsilon_{\rm DM,c}$ and $\epsilon_{\rm gas,c}$ indicate the comoving Plummer-equivalent gravitational softening length for DM particles and gas particles, respectively, $\epsilon_{\rm DM,p}$ and $\epsilon_{\rm gas,p}$ indicate the physical maximum Plummer-equivalent gravitational softening length for DM and gas particles, respectively. In works using moving mesh codes, such as Bourne & Sijacki (2021), $r_{\rm cell}$ indicates the cell radius.

Simulation set-up	Model	Reference	$m_{\rm DM}$ ($\rm M_\odot$)	$m_{\rm gas}$ ($\rm M_\odot$)	$\epsilon_{\rm DM,c}$ (ckpc)	$\epsilon_{\rm gas,c}$ (ckpc)	$\epsilon_{\rm DM,p}$ (pkpc)	$\epsilon_{\rm gas,p}$ (pkpc)	Produces cool cores?
Group and cluster (low-res)	SWIFT-EAGLE	Altamura et al. (2023)	7.85×10^7	1.47×10^7	6.66	3.80	2.96	1.69	No
Group and cluster (mid-res)	SWIFT-EAGLE	Altamura et al. (2023)	9.82×10^6	1.83×10^6	3.33	1.90	1.48	0.854	No
Group (high-res)	SWIFT-EAGLE	This work	1.23×10^6	2.29×10^5	1.67	0.95	1.74	0.427	No
Group and cluster (low-res)	Non-radiative	This work	7.85×10^7	1.47×10^7	6.66	3.80	2.96	1.69	Yes
Group and cluster (mid-res)	Non-radiative	This work	9.82×10^6	1.83×10^6	3.33	1.90	1.48	0.854	Yes
Group (high-res)	Non-radiative	This work	1.23×10^6	2.29×10^5	1.67	0.95	1.74	0.427	Yes
Two groups and cluster*	SWIFT-EAGLE†	Nobels et al. (2022)	–	$(1-42) \times 10^5$	–	–	–	0.30	Yes
Two groups and cluster*	SWIFT-EAGLE‡	Huško et al. (2022)	–	$(1-42) \times 10^5$	–	–	–	0.30	Yes
EAGLE 100 Mpc (Ref)	EAGLE Ref	Schaye et al. (2015)	9.60×10^6	1.80×10^6	–	–	–	0.700	No
EAGLE 25 Mpc (high-res)	EAGLE Ref	Schaye et al. (2015)	1.21×10^6	2.26×10^5	–	1.33	–	0.350	No
C-EAGLE/Hydrangea	EAGLE-AGNdT9	Barnes et al. (2017b)	9.60×10^6	1.80×10^6	–	–	–	0.700	No
TNG50	TNG	Nelson et al. (2019)	4.50×10^5	8.50×10^4	0.288	0.074	–	–	No
TNG300 + TNG-Cluster	TNG	Nelson et al. (2024)	6.1×10^7	1.2×10^7	1.480	0.370	–	–	Yes^a
SIMBA (m100n1024)	SIMBA	Davé et al. (2019)	9.6×10^7	1.82×10^7	0.74	0.74	–	–	No
FABLE (clusters)	FABLE	Henden et al. (2018)	8.1×10^7	9.4×10^6	4.142	4.142	4.142	4.142	No
ZCool_SF_SN_AGN (groups)	cosmo-OWLS	McCarthy et al. (2011)	5.56×10^8	1.18×10^8	10.7	10.7	2.74	2.74	Yes
MACSIS (390 custers)	BAHAMAS	Barnes et al. (2017a)	6.49×10^9	1.18×10^9	5.9	5.9	5.9	5.9	Yes
BAHAMAS (groups)	BAHAMAS	McCarthy et al. (2017)	5.50×10^9	1.09×10^9	5.7	5.7	5.7	5.7	Yes
FLAMINGO (m9)	FLAMINGO	Schaye et al. (2023)	5.65×10^9	1.07×10^9	22.3	22.3	5.70	5.70	Yes^b
ROMULUS-C	ROMULUS	Tremmel et al. (2019)	3.40×10^5	2.10×10^5	–	–	–	0.250	Yes
Groups *c10kHR**	Kinetic feedback	Barai et al. (2016)	–	2.13×10^6	–	–	–	1.40	Yes
Cluster	Fiducial jet-AGN	Bourne & Sijacki (2021)	6.86×10^7	1.94×10^7	–	–	$2.5\, r_{\rm cell}$	4.00	Yes
Perseus-like cluster*	XMAGNET	Grete et al. (2025)	–	–	–	–	–	0.0977	Yes

Notes. *Indicates full-physics simulations of isolated halos, with the highest particle-mass resolution in the inner 100 kpc and quadratically degrading resolution out to r_{500}, except for Barai et al. (2016), where the particle mass is fixed inside r_{500}, and for Grete et al. (2025), where the maximally refined region spans 125 kpc. The DM halo is modelled with an external potential following a Navarro–Frenk–White profile (Navarro, Frenk & White 1997).
†The EAGLE-like model differs from Altamura et al. (2023) in the black-hole accretion and the star formation scheme.
‡The EAGLE-like model implements the changes of Nobels et al. (2022), and models AGN feedback using self-consistent jets (Huško et al. 2022). The CC/NCC abundances and entropy profiles are documented in: ^{a}Lehle et al. (2024) and ^{b}Braspenning et al. (2024).

manifests as an entropy floor in radial profiles. Specifically, the low-entropy gas subject to cooling was shown to be preferentially heated by AGN feedback and then ejected from the system (McCarthy et al. 2011). In the same work, SNe feedback was shown to regulate the entropy truncation in OWLS protogroups and protoclusters. SN can moderate the cooling of the gas at high redshift, thus preventing the removal of low-entropy gas by star formation too early and without shifting the median entropy of the IGM.

The subgrid model in McCarthy et al. (2011) that included metal cooling, star formation, and feedback (denoted *ZCool_SF_SN_AGN*, as part of the OWLS suite of simulations, Schaye et al. 2010) successfully reproduced X-ray properties of galaxy groups, including entropy, temperature, and density distributions, as well as their halo-mass dependence. In addition to full-physics simulations, the study presented NR runs (labelled as *NoCool*), where baryonic physics was switched off. By comparing thermodynamic properties of gas particles inside r_{500}[2] in *NoCool* with their counterparts in full-physics runs, McCarthy et al. (2011) could identify the gas in ZCool_SF_SN_AGN that had been ejected as a direct consequence of feedback. Reportedly, the gas ejected from the progenitors of the halo at high redshift ($z > 1$) forms the high-entropy phase, while the remaining gas, albeit hot, allows the self-regulation of heating and cooling and the formation of stable CCs.

Moreover, the increase in entropy in the hot halo gas in ZCool_SF_SN_AGN is due to two factors: first, the low-entropy gas can be directly and selectively heated by the central supermassive black hole (cSMBH) and ejected from the system, allowing higher entropy gas to flow inwards to replace it; second, low-entropy gas can quickly cool and form stars, resulting in the low-entropy gas phase being further depleted. These processes have their biggest impact on low-mass progenitor haloes, particularly at redshifts $z \approx 2$–4, and dictate which systems can develop a stable CC and which ones will be turned into NCC. Overall, the OWLS simulations (McCarthy et al. 2010), as well as cosmo-OWLS (Le Brun et al. 2014) and BAHAMAS (McCarthy et al. 2017), produced steep, power-law-like entropy profiles and realistic hot gas fractions simultaneously on group scales. In the simulations of Paper I, the entropy amplification appears to have been vastly more intense, removing most of the inner IGM gas from the low-entropy phase and inhibiting the formation of stable CCs by $z = 0$.

In this paper, we take a further step in the analysis of the group and cluster of Paper I by examining the evolution of their properties and entropy distribution. Using time-series data, we capture the state of the group and cluster systems when the central entropy increased and characterize the processes that may have seeded the plateau in the entropy profiles. By introducing a simulation of the group at a resolution eight times higher than EAGLE (labelled as high-res), we

[2] r_Δ is the radius at which the internal mean density exceeds the critical density of the Universe by a factor of Δ. This approach defines r_{500} for $\Delta = 500$ and r_{200} and for $\Delta = 200$ (conventionally taken as the virial radius). M_Δ is defined as the total mass within a spherical overdensity of radius r_Δ centred in the gravitational potential minimum.

show that entropy plateaus persist as subgrid physics is resolved on smaller scales. Notably, to our knowledge, our high-res group is one of the highest resolution full-physics simulations evolved to $z = 0$ of an object on group scales (the HR group in Richings et al. 2021 was run with a similar resolution). We divide our analysis into two sections:

(i) First, we analyse 3D aperture properties and entropy profiles during three key phases of the evolution of the two objects. This approach is similar to the study on the ROMULUS-C cluster (Tremmel et al. 2017; Chadayammuri et al. 2021).

(ii) Second, we introduce the NR group and cluster simulations (see Table 1). By selecting matching gas particles in the NR and Ref runs, we reconstruct the thermodynamic Lagrangian history of the gas in the core ($r < 0.15\,r_{500}$), the entropy-plateau region ($0.15 < r/r_{500} < 1$), and the surrounding environment ($1 < r/r_{500} < 6$). The goal of this analysis is to verify the extent to which the ejection scenario described by McCarthy et al. (2011) applies to our simulations.

This work is structured as follows. In Section 2, we summarize the set-up and subgrid models of the simulations used in our study. Then, in Section 3, we illustrate the analysis techniques and define the key physical quantities. Section 4 contains the results with the evolution of basic properties and thermodynamic profiles, the Lagrangian histories and distributions of selected subsets of gas particles. Finally, we discuss and summarize the results in Section 6. Throughout this work, we assume the *Planck* 2018 cosmology, given by $\Omega_{\rm m} = 0.3111$, $\Omega_{\rm b} = 0.04897$, $\Omega_\Lambda = 0.6889$, $h = 0.6766$, $\sigma_8 = 0.8102$, $z_{\rm reion} = 7.82$, and $T_{\rm CMB} = 2.7255$ K (Planck Collaboration VI 2020).

2 SIMULATED GROUP AND CLUSTER

In this analysis, we use the simulated group and cluster in Paper I, run with the Ref and NR models. This section summarizes the key properties of the simulation technique and the properties of the two systems.

2.1 Zoom-in simulation technique and set-up

The group and cluster objects are selected from a $(300\ {\rm Mpc})^3$ dark-matter-only volume at $z = 0$. By choice, these halos are relatively isolated systems, as they are not surrounded by any other object with a mass above 10 per cent of their mass within a $10\,r_{500}$ radius. The group has a mass $M_{500} = 8.83 \times 10^{12}$ M$_\odot$ at $z = 0$, and was randomly selected from the low-mass subset of Paper I. It is representative of small galaxy assemblies a few times more massive than the Local Group ($M \approx 4 \times 10^{12}$ M$_\odot$, Benisty et al. 2022). Going to higher masses, the cluster has $M_{500} = 2.92 \times 10^{14}$ M$_\odot$ at $z = 0$ and was randomly selected from the high-mass bin. The cluster is representative of a system about 3.5 times more massive than the Virgo galaxy cluster ($M_{500} \approx 0.83 \times 10^{14}$ M$_\odot$, Simionescu et al. 2017) or half the mass of the Coma galaxy cluster ($M_{500} \approx 6 \times 10^{14}$ M$_\odot$, Mirakhor & Walker 2020).

To model the group and cluster, we follow the zoom-in simulation technique, which consists of refining the numerical resolution inside a defined volume of interest and degrading the resolution elsewhere (Katz & White 1993; Tormen, Bouchet & White 1997). By concentrating the resolution elements in the region of interest, the zoom-in method is particularly efficient at modelling individual objects with moderate computational cost. The zoom-in initial conditions are generated in three steps:

(i) The high-resolution region is chosen to be a $6\,r_{500}$ sphere, centred on the potential minimum at $z = 0$. The positions of the dark matter (DM) particles in this volume are then tracked back to the initial conditions at $z = 127$ using their unique IDs.

(ii) The Lagrangian volume enclosing the selected particles at $z = 127$ is masked, in preparation for the high-resolution particle load. In some instances, the Lagrangian domain presents concave subregions, such as gaps or holes. We extrude the mask boundaries until the main concavities are filled to minimize the chances of contamination from low-resolution DM-filled gaps. This technique is referred to as topological closure and is described in chapter 3 of Altamura (2023). With topological closure, the number of high-resolution DM particles increases by $1 - 5$ per cent to fill the extra padding around the Lagrangian volume. Despite a slightly longer runtime, the additional refinement leads to a nearly contamination-free volume out to $6\,r_{500}$.

(iii) The displacement and velocity fields are computed using PANPHASIA (Jenkins 2013) and IC_GEN, a FORTRAN code that implements the method of Jenkins (2010) to generate realizations of primordial Gaussian random fields in a multiscale setting.[3]

The initial conditions for the group and cluster are produced at three resolutions, labelled 'low', 'mid', and 'high', summarized in Table 1 (highlighted). The mid-resolution is the same as for the EAGLE L100N1504 volume from Schaye et al. (2015), characterized by dark matter particles with mass $m_{\rm DM} = 9.82 \times 10^6$ M$_\odot$ and initial gas particle mass $m_{\rm gas} = 1.83 \times 10^6$ M$_\odot$. With a mass resolution eight times lower than EAGLE, the low-resolution setup has eight times larger (initial) particle masses. Finally, the high-resolution setup has eight times smaller particle masses, making it eight times higher resolution than the EAGLE L100N1504 volume. Table 1 also reports the corresponding comoving and physical Plummer-equivalent gravitational softening length for DM and gas particles associated with the three resolutions.

We run dark-matter-only simulations of the two objects at all resolutions to check for contaminating low-resolution (i.e. boundary) dark matter particles used to define the tidal field around the high-resolution region within the $6\,r_{500}$ clean radius. At $z = 0$, the contaminating mass within $6\,r_{500}$ was at most 0.1 per cent, with no boundary particles within r_{500}.

2.2 The SWIFT-EAGLE reference model

We summarize the features of the SWIFT-EAGLE Ref model, referring to Paper I for a full discussion. As in the original EAGLE Ref model of Schaye et al. (2015), the thermodynamics of the ISM is governed by a pressure floor (Schaye & Dalla Vecchia 2008). The hydrodynamics of the gas is modelled using the smoothed-particle hydrodynamics (SPH) approach, particularly suited for describing systems with a vast density dynamic range, such as galaxy formation environments. The simulations were run with SWIFT configured with the SPHENIX (Borrow et al. 2022) hydrodynamic scheme. SPHENIX implements the 'traditional' density-energy method, in addition to artificial conduction and artificial viscosity.

The gas cooling process is governed by the Ploeckinger & Schaye (2020) cooling tables. This prescription accounts for a redshift-dependent ultraviolet (UV)/X-ray background from Faucher-Giguère

[3]The phase descriptor containing the unique seed of the white noise field used for the parent simulation and the zoom simulations is [Panph1, L18, (74412, 22732, 260484), S3, CH1799108544, EAGLE − XL_L0300_VOL1].

(2020), self-shielding for the cool ISM, presence of dust, interstellar radiation field, and cosmic rays via the Kennicutt–Schmidt relation (Kennicutt 1998). When cold and dense gas reaches the equation of state of the pressure floor, it is converted into stars. Star formation is modelled as a subgrid process. It uses a Kennicutt–Schmidt-like pressure law (Schmidt 1959; Kennicutt 1998; Schaye & Dalla Vecchia 2008) and a metallicity-dependent number density threshold (Schaye 2004; Crain et al. 2015), above which gas turns into stars.

Each star particle represents a simple stellar population (SSP), which contributes to the chemical enrichment of the surrounding gas via the subgrid treatment of three stellar wind channels (Wiersma et al. 2009): asymptotic giant branch and massive stars, core-collapse supernovae (SNII) and type-Ia supernovae (SNIa, Schaye et al. 2015). Assuming a Chabrier (2003) initial mass function populated by stars between 0.1–100 $M_\odot$, we consider all massive stars above 8 $M_\odot$ to end their life with SNII episodes. In each time-step, the expected number of SNII events, each releasing 10^{51} erg of energy, is computed. Notably, the probabilistic approach of this calculation makes our SN feedback implementation stochastic. Finally, the total energy is then injected thermally into a small number of neighbouring gas particles, as prescribed by Dalla Vecchia & Schaye (2012). During this step, the temperature of gas particles involved in the feedback is raised by $\Delta T_{\rm SN} = 10^{7.5}$ K. The gas particles to heat are chosen to be closest to the SSP, as prescribed by the minimum-distance energy distribution scheme (Paper I).

The feedback from AGN is powered by SMBHs, seeded at $z \leq 19$ in groups above a friends-of-friends (FoF) mass of $M_{\rm FoF} = 10^{10}\,M_\odot$. With an initial mass set to $M_{\rm seed} = 10^4\,M_\odot$, (supermassive) BHs are positioned at the gas density maximum. Subsequently, they can grow by accreting surrounding gas or merging with other BHs.

Using the spherically symmetric Bondi–Hoyle–Lyttleton model (Hoyle & Lyttleton 1939; Bondi & Hoyle 1944), the mass accretion rate is expressed as

$$\dot{m}_{\rm BH} = \alpha\,\frac{4\pi G^2\, m_{\rm BH}^2\,\rho_{\rm gas}}{\left(c_{\rm s}^2 + v_{\rm gas}^2\right)^{3/2}}, \tag{1}$$

where $m_{\rm BH}$ is the BH subgrid mass, $c_{\rm s}$ is the gas sound speed, $v_{\rm gas}$ the bulk velocity of the gas in the kernel relative to the BH, and $\rho_{\rm gas}$ the gas density evaluated at the BH position. The SWIFT-EAGLE BH accretion model does not require boosting (Booth & Schaye 2009) because of the sufficiently high gas density around the BHs. Therefore, the boost factor is $\alpha = 1$. We do not apply an Eddington limiter to the mass accretion rate to allow for realistic quasar-mode accretion, and, similarly to the AGN feedback in the EAGLE-like model in Nobels et al. (2022), we do not include the Rosas-Guevara et al. (2015) angular momentum limiter. Finally, we measure $\dot{m}_{\rm BH}$ in units of the Eddington (1926) accretion rate, which scales linearly with BH mass: $\dot{m}_{\rm Edd} \propto m_{\rm BH}$.

Our AGN feedback mechanism is deterministic and uses an energy reservoir to trigger the energy injection. A fraction $\epsilon_{\rm r} = 0.1$ (radiative efficiency from Shakura & Sunyaev 1973) of the mass accreted by the BH is converted into energy, and a fraction $\epsilon_{\rm f} = 0.1$ of that energy is then accumulated in the reservoir. When the reservoir contains enough energy to raise the temperature of a designated gas neighbour by $\Delta T_{\rm AGN}$ (Booth & Schaye 2009), an AGN feedback event occurs. In the Ref model, the temperature of the target gas particle is raised by $\Delta T_{\rm AGN} = 10^{8.5}$ K, fixed for all AGN feedback events. The single gas particle to heat per feedback event is chosen to be closest to the BH, in analogy with the SN feedback scheme. In summary, this AGN feedback scheme is purely thermal (no kinetic energy is directly transferred to the gas) and deterministic. To compensate for the unresolved dynamical friction, BHs need to be artificially re-positioned towards the gravitational potential minimum (`Default` method of Bahé et al. 2022). This algorithm prevents the BHs from drifting away from the centre of galaxies into low-density environments, where they would grow unnaturally slowly and generate little feedback activity. Unlike the repositioning method of Paper I, the target potential minimum is obtained excluding the contribution of the BH to the local gravitational potential. This change improves the stability of the algorithms by reducing the risk of high-mass BHs drifting towards self-induced gravitational potentials. With the BHs stably located in high-density environments, we expect their final mass to be higher and the AGN feedback stronger than in Paper I.

2.3 The non-radiative model

To directly assess the impact of baryonic processes, we rerun our group and cluster with photoheating, but switching off radiative cooling. Star formation, BH seeding, and feedback are not included either. This configuration, describing a model that only includes gravity, gas hydrodynamics, and a photoionizing UV/X-ray background (Faucher-Giguère 2020), is referred to as an NR model. As in McCarthy et al. (2011), we use this model of the group and cluster to track identical particles to that in Ref to probe the effects of baryonic processes on the IGM (see Section 5).

3 ANALYSIS METHODS

Our study employs two types of analysis. The first type, used in Section 4, defines the global properties of the objects within r_{500} and the radial profiles, sampled at different snapshots throughout the simulation; we describe these properties in Section 3.1. The second type is based on selecting identical sets of particles using their unique IDs, as required to construct the Lagrangian thermal histories presented in Section 5; we describe this technique in Section 3.2.

3.1 IGM properties

We define the gas mass, $M_{\rm gas}$, by adding the mass of the gas particles within r_{500}

$$M_{\rm gas} = \sum_{i:r<r_{500}} m_{g,i}, \tag{2}$$

where r is the Euclidean distance from the potential minimum and $m_{g,i}$ is the mass of the ith gas particle. This ensemble of particles is also subject to a temperature selection criterion depending on whether the hot or cold gas mass is computed. The stellar mass $M_\star$ is obtained similarly, but replacing the gas-particle mass with the star particle mass $m_{\star,i}$.

The entropy calculation follows Paper I. First, we obtain the number density of free electrons accounting for the chemical abundances from the chemical elements tracked by the subgrid model. Assuming fully ionized gas, we define the total free-electron fraction for each hot ($T > 10^5$ K) gas particle as

$$X_{\rm e} \equiv \frac{n_{\rm e}}{n_{\rm H}} = \frac{m_{\rm H}}{f_{\rm H}} \sum_\epsilon Z_\epsilon \frac{f_\epsilon}{m_\epsilon} \tag{3}$$

and the ion fraction X_i

$$X_{\rm i} \equiv \frac{n_{\rm i}}{n_{\rm H}} = \frac{m_{\rm H}}{f_{\rm H}} \sum_\epsilon \frac{f_\epsilon}{m_\epsilon}, \tag{4}$$

which can be combined to compute the electron number density

$$n_{\rm e} = \frac{X_{\rm e}}{X_{\rm e} + X_{\rm i}} \frac{\rho_g}{\mu\, m_{\rm H}} = \rho_g \sum_{\epsilon} Z_{\epsilon} \frac{f_{\epsilon}}{m_{\epsilon}}, \tag{5}$$

where f_{ϵ} is the gas-particle mass fraction for chemical element $\epsilon = \{\rm H, He, C, N, O, Ne, Mg, Si, S, Ca, Fe\}$, m_{ϵ} the associated atomic mass and Z_{ϵ} the atomic number. $f_{\rm H}$ and $m_{\rm H}$ are the hydrogen mass fraction and atomic mass respectively. Then, ρ_g is the SPH density of the gas particle and μ its mean atomic weight, computed by combining the contribution from the chemical species as

$$\mu = \left[m_{\rm H} \sum_{\epsilon} \frac{f_{\epsilon}}{m_{\epsilon}} (Z_{\epsilon} + 1) \right]^{-1}. \tag{6}$$

For our results, we present entropy, mass-weighted (MW) temperature and density profiles of the simulated groups and clusters. To compute the radial profiles, we consider 50 spherical shells centred on the halo's centre of potential with a logarithmically increasing radius, spanning $(0.01 - 2.5)\, r_{500}$. We then sum the contributions of the particles within each radial bin. For the ith shell, we compute the density profile as

$$\rho_{g,i} = \frac{\sum_j m_j}{V_i}, \tag{7}$$

where the sum is the total gas mass in shell i, divided by the volume V_i of the shell. We also define the MW temperature $T_{{\rm MW},i}$ as

$$T_{{\rm MW},i} = \frac{\sum_j m_j T_j}{\sum_j m_j}. \tag{8}$$

The entropy profiles are then computed via the MW temperature profiles and the density profiles, as described in Vikhlinin et al. (2006)

$$K(r) = \frac{{\rm k_B} T(r)}{n_{\rm e}(r)^{2/3}}. \tag{9}$$

The entropy profiles are normalized to their self-similar values, appropriate for an atmosphere in hydrostatic equilibrium. The normalization is obtained in three steps. First, we define the critical density of the universe as

$$\rho_{\rm crit}(z) = E^2(z) \frac{3H_0^2}{8\pi G}, \tag{10}$$

where $E^2(z) \equiv H^2(z)/H_0^2 = \Omega_{\rm m}(1+z)^3 + \Omega_{\Lambda}$. To select X-ray-emitting gas, we only consider gas particles above a temperature of 10^5 K. Secondly, we compute the characteristic temperature at r_{500},

$$k_{\rm B} T_{500} = \frac{G \bar{\mu} M_{500} m_{\rm H}}{2\, r_{500}}, \tag{11}$$

where $\bar{\mu} = 0.5954$ is the mean atomic weight for an ionized gas with primordial ($X = 0.76$, $Z = 0$) composition. Finally, using the characteristic temperature and density ($500\, \rho_{\rm crit}$), we establish the characteristic entropy:

$$K_{500} = \frac{k_{\rm B} T_{500}}{\left[500\, f_{\rm bary} \rho_{\rm crit} / (\overline{\mu}_{\rm e} m_{\rm H})\right]^{2/3}}, \tag{12}$$

where $\overline{\mu}_{\rm e} = 1.14$ is the mean atomic weight per free electron and $f_{\rm bary} = 0.157$ is the universal baryon fraction obtained by Planck Collaboration VI (2020).

3.2 Matched particle ensembles

Selecting particles using only a spatial mask, such as the $r < r_{500}$ criterion for the cluster properties, does not guarantee that the set contains the same particles between different snapshots. In fact, within this mask, gas particles are regarded as indistinguishable. Crucially, baryonic particles are expected to be displaced at almost every time-step, following the equations of motion, e.g. SPH particles (Borrow et al. 2022), or repositioning algorithms, i.e. SMBHs (Bahé et al. 2022).

To characterize the thermodynamic history of the particles that describe the IGM today, it is necessary to select identical particles unequivocally, which can be achieved only if they are distinguishable. In SWIFT, particles can be distinguished by their unique ID, a long-integer value assigned to each particle at the start of the simulation and never altered. Using particle IDs, our selection strategy is described as follows. First, we generate a list containing the unique IDs of particles that satisfy given criteria at $z = 0$; we denote this set as the master list. Secondly, we search for particles in a different snapshot whose ID appears in the master list. This technique was introduced in McCarthy et al. (2011) to construct the Lagrangian history of sets of unique particles and track their thermodynamic state through redshift. Similar methods employing massless tracers were successful in tracking fluid elements in mesh-based simulations to study the entropy core in galaxy clusters via velocity-field tracers (Vazza 2011) or Monte Carlo tracers (Genel et al. 2013). In all our SPH simulations, we adopt the method by McCarthy et al. (2011) with additional selection criteria, as described below.

Throughout this work, particles selected at $z = 0$ are required to be in the hot, X-ray-emitting phase, i.e. above 10^5 K. For instance, in the case of a selection by particle ID on the present-day Ref snapshot we denote this selection as $\mathrm{ID}_{\rm Ref}(z = 0, T > 10^5\ \mathrm{K})$. Since we always select particles by ID, we can abbreviate this notation as $\mathcal{A}_{\rm Ref} = \mathrm{Ref}(z = 0)$. Following this logic, the particles from any snapshot are represented as $\mathcal{B}_{\rm Ref} = \mathrm{Ref}(z \geq 0)$. Note that no temperature cut is imposed on the $z > 0$ snapshots since we only require the gas 'parcels' to be in the X-ray-emitting phase at the present day. The particle tracking is performed by searching the particle IDs in $\mathcal{B}$ that also appear in $\mathcal{A}$, expressed as follows:

$$\mathcal{B}_{\rm Ref} \in \mathcal{A}_{\rm Ref} \equiv \mathrm{Ref}(z \geq 0) \in \mathrm{Ref}(z = 0, T > 10^5\ \mathrm{K}). \tag{13}$$

Provided that the initial conditions are identical, the comparison between snapshots is not restricted to the same simulation but can be performed between different runs, here Ref and NR. In our study, we consider four combinations, described as follows.

(i) $\mathcal{B}_{\rm Ref} \in \mathcal{A}_{\rm Ref}$. This choice selects the particles at $z = 0$ in Ref and tracks them back in time in the Ref model.
(ii) $\mathcal{B}_{\rm NR} \in \mathcal{A}_{\rm NR}$ operated as the case above but for the NR model.
(iii) $\mathcal{B}_{\rm NR} \in \mathcal{A}_{\rm Ref}$. This choice selects particles in Ref at $z = 0$ but tracks them throughout redshift in NR.
(iv) $\mathcal{B}_{\rm Ref} \in \mathcal{A}_{\rm NR}$. Now, we select particles in NR but then track them throughout redshift in Ref. This procedure is analogous to the previous one, but swapping the model indices: NR $\leftrightarrow$ Ref.

By construction, the master list in Ref excludes particles that formed stars or were swallowed by BHs. Therefore, the gas at higher redshift that is destined to be converted into other particle types or energy does not feature in the Lagrangian histories built with our prescription. The same is done when matching particles between different models: the master list for case (iv) also excludes NR particles that do not have a Ref counterpart at $z > 0$ due to star formation or BH accretion, i.e. the list only includes particles whose

ID exists in both lists. This restriction is not necessary in case (iii) because no gas particles are lost in the NR scenario, where subgrid physics is switched off. To simplify the ID tracking, we exclude the gas particles that have undergone splitting, implemented in SWIFT to prevent particles from becoming very massive when they have absorbed a large amount of stellar mass loss. We do not expect this approximation to affect the Lagrangian history since the gas particles involved in splitting are < 0.1 per cent of the ensemble for the simulation with the most splitting events (high-res group).

Since we aim to investigate the shape of the entropy profile (and not just the entropy level), we split the $z = 0$ selection into three independent spherical regions, as follows:

(i) *Core*. This master list includes particles that end up hot in the core, as defined by the additional spatial mask: $T > 10^5$ K $\wedge\, r < 0.15\, r_{500} \wedge z = 0$.

(ii) *Shell*. This master list includes hot particles within the IGM, but located outside the core: $T > 10^5$ K $\wedge\, 0.15 < r/r_{500} < 1 \wedge z = 0$. The shell surrounding the core appears to contain hot gas with approximately similar entropy, which we identify as an entropy plateau in radial profiles.

(iii) *Outskirts*. Lastly, we select hot particles that end up outside the group or cluster, i.e. $r > r_{500}$. We restrict the outer boundary to the clean refined region in the zoom-in simulation, which is $6\, r_{500}$ at $z = 0$. Thus, the constraints for this master list are: $T > 10^5$ K $\wedge\, 1 < r/r_{500} < 6 \wedge z = 0$.

4 REDSHIFT EVOLUTION

We present results from the evolution history of the group and cluster in four parts: first, we show the evolution of useful properties and, based on them, identify three key phases; second, we qualitatively illustrate the shift from cold- to hot-gas-dominated IGM; third, we focus on the evolution of the baryon content (quantitatively); and fourth, we link the above results to the scaled entropy profiles.

4.1 Basic properties

In Fig. 1, we show the evolution of the halo mass (M_{500}), the specific star formation rate (sSFR) in Gyr^{-1}, the BH mass (in M$_\odot$), and BH mass accretion rate (BHMAR) in units of the Eddington rate $\dot{m}_{\rm Edd}$ computed for the central BH only. These quantities are defined as follows. M_{500} is the total mass within r_{500}, as discussed previously. The sSFR is computed using star particles within a 50 kpc spherical aperture and using stars formed in the 50 Myr before the snapshot. At $z = 0$ (local Universe), we call the brightest central galaxy (BCG) quenched if its sSFR is below the quenched threshold of 10^{-2} Gyr^{-1}, indicated by a grey triangle (Piotrowska et al. 2022, from Sloan Digital Sky Survey Data Release 7, SDSS DR7, galaxies with stellar mass between $10^9 - 10^{12}$ M$_\odot$ and halo mass $> 10^{11}$ M$_\odot$). At high redshift ($z > 0.5$), we use two redshift-dependent quenched thresholds, defined as $1/t_{\rm H}(z)$ (dashed grey) and $1/3t_{\rm H}(z)$ (dotted–dashed grey). These were shown to be effective in classifying active and quenched galaxies in the ILLUSTRISTNG (Tacchella et al. 2019) and *James Webb Space Telescope* (*JWST*)-CEERS samples (Bluck et al. 2024) up to $z = 7.5$ and 6.5, respectively (for *JWST*-CEERS observations, higher redshift bins contain too few quenched galaxies to estimate a threshold reliably, see also Bluck, Piotrowska & Maiolino 2023). The Eddington accretion rate (Eddington 1926) used to scale the BHMAR is defined for a spherically symmetric matter distribution as

$$\dot{m}_{\rm Edd} = \frac{4\pi G m_{\rm P}}{\epsilon_{\rm r}\, c\, \sigma_{\rm T}}\, m_{\rm BH} \approx 2.218\ {\rm M}_\odot\ {\rm yr}^{-1}\ \frac{\epsilon_{\rm r}}{0.1}\ \left(\frac{m_{\rm BH}}{10^8\ {\rm M}_\odot}\right). \quad (14)$$

We track the progenitor of the main halo at $z = 0$ by taking the object with the largest $M_{\rm FoF}$ in the high-resolution volume at $z > 0$. Here, we use halo centres computed with the VELOCIRAPTOR structure-finding code configured with the 6D FoF algorithm (Elahi et al. 2019). We found this method sufficient for tracking the central object's progenitors over most of the redshift range, as shown qualitatively by the M_{500} evolution in Fig. 1. Occasionally, the mass jumps to lower values when a secondary halo near the central one becomes the most massive for a short time. These inaccuracies do not affect the redshift-evolution results. In Section 4.4, we manually excluded the affected snapshots within the redshift bands from the analysis. The results of Section 5 are unaffected because they only use unique particle IDs selected at $z = 0$.

We identified three evolutionary phases, summarized in Table 2 and described below.

(i) Phase A (quasar mode) spans $z = 1.5 - 3.0$ $(2.2 - 4.0)$ for the group (cluster) and captures the peak of AGN activity. During this period, the protogroup is a galaxy with a median mass $M_{500} = 1.38 \times 10^{12}$ M$_\odot$ in rapid growth. The BCG experiences intense star formation, which sharply declines below the $1/3t_{\rm H}(z)$ quenched threshold by the end of the phase as the central BH's mass accretion rate approaches $\dot{m}_{\rm Edd}$. The protocluster's mass increases rapidly to that of a fully formed galaxy (median $M_{500} = 5.31 \times 10^{12}$ M$_\odot$). During this phase, the central BH also grows rapidly, and its AGN feedback will later lead to the shutdown of star formation in the BCG.

(ii) Phase B spans $z = 0.7 - 1.3$ $(1.5 - 2.0)$ for the group (cluster) and captures merger events which further increase M_{500}. In both objects, the sSFR of the BCG fluctuates between $10^{-1} - 10^0$ Gyr^{-1}; the central BH's mass increases.

(iii) Phase C represents the quenched state of the systems near the present time ($0 \le z < 0.3$). The group shows a decrease in M_{500}, followed by an increase due to the infall of a substructure, correlating with an increase in sSFR. The BHMAR remains just below $\approx 10^{-3}\, \dot{m}_{\rm Edd}$. The cluster also experiences a mass accretion event at low redshift. By the end of phase C, both the group and cluster central BHs are in radio mode, defined by BHMAR $< 10^{-3}\, \dot{m}_{\rm Edd}$ (e.g. Hopkins & Hernquist 2009).

The metrics for the group and the cluster at different resolutions are broadly consistent throughout the simulation, indicating good numerical convergence. However, we find that the sSFR of the BCG in the group at low-res is higher than for the other two resolutions by up to 1 dex between $z = 1 - 2$ (phase B). This is because the central BH is less massive compared to mid- and high-res during that time, and therefore the feedback it produces is less effective in quenching star formation.

The brief dips in M_{500} are artefacts of the VELOCIRAPTOR structure-finding code, which picked the wrong halo as the central during the merger of similar-mass objects. This effect could be corrected using merger-tree information; however, this operation is unnecessary for our study, as the artefacts do not affect our conclusions. The gaps in sSFR at redshift 10 or higher indicate periods where no BCG-associated stars formed within a 50 Myr window.

We summarize the insights from Fig. 1 as follows. The growth of the group and cluster progenitors via mergers favours the BH growth. Consequently, this intensifies the AGN activity, leading to a drop in sSFR below the quenching threshold in (part of) phase B. This result supports previous work that correlates the growth of BHs with merger activity (Kulier et al. 2015) and the BH self-regulation mechanism (Maiolino et al. 2012; Nobels et al. 2022). Moreover, these events are more noticeable in the group progenitor than the cluster progenitor.

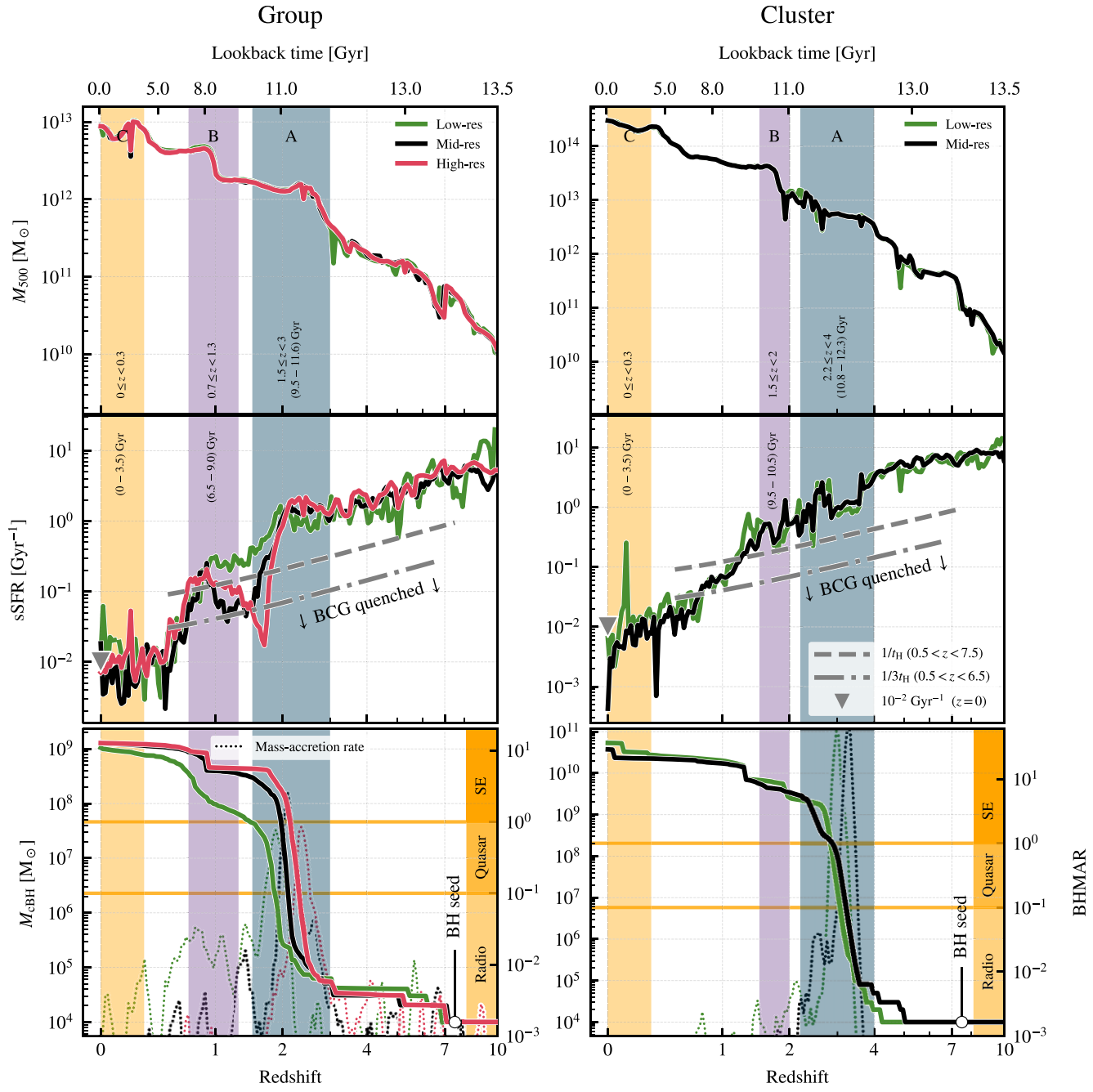

Figure 1. Evolution of the mass (M_{500}, top row), the sSFR (middle row) in a physical 50 kpc aperture, and the mass of the central BH (cBH, bottom row) with redshift, z, and lookback time (top axis). Left: properties of the group at low (green), mid (black), and high (red) resolution. Right: properties of the cluster at low (green) and mid (black) resolution. The three phases are indicated with coloured bands, with the intervals reported in terms of redshift (top row) and lookback time (middle row). The intervals are fixed for both objects. We indicate sSFR= 10^{-2} Gyr^{-1}, below which we consider the BCG quenched, with a grey triangle at $z = 0$ (Piotrowska et al. 2022). We also show two quenching threshold definitions at high redshift: $1/t_H(z)$, where $t_H(z)$ is the redshift-dependent *Hubble* time, for $0.5 < z < 7.5$ (dashed grey), and $1/3t_H(z)$ for $0.5 < z < 6.5$ (dotted–dashed grey, Tacchella et al. 2019; Bluck et al. 2024). In the bottom row, we highlight the seed mass of the central BH, $M_{cBH} = 10^4$ $M_\odot$. The dotted lines are the BHMAR in units of the Eddington rate, averaged over ten rolling snapshots using a Savitzky–Golay filter with a degree-3 polynomial basis (Savitzky & Golay 1964). The BHMAR scale is shown on the right. The horizontal yellow lines are the threshold BHMAR that defines the AGN to be in radio mode, BHMAR $< 10^{-3}\,\dot{m}_{Edd}$, quasar mode, $10^{-3} \leq$ BHMAR$/\dot{m}_{Edd} < 1$, and super-Eddington (SE) mode, BHMAR $\geq \dot{m}_{Edd}$.

4.2 Transition from the cold to hot IGM

The evolution of the IGM gas temperature is key to understanding the entropy distribution and the baryon content. In Fig. 2, we illustrate temperature and entropy maps for the high-res group and the mid-res cluster at three redshifts within each phase, as indicated to the left of the panels. The columns show the following quantities, from left to right. The projected mass ratio, R_i, is evaluated by summing the

Table 2. Summary of the three phases of the evolution of the group and cluster considered in this work. We report the redshift (z) and lookback time (t, in Gyr) intervals with a description of the event or physical state characterizing each evolutionary phase. The phase description is colour-coded as in the rest of the document; the z and t ranges are highlighted in alternating colours for readability.

Phase	Description		Group	Cluster
A	Quasar mode	z	1.5 – 3.0	2.2 – 4.0
		t	9.5 – 11.6	10.8 – 12.3
B	Merger	z	0.7 – 1.3	1.5 – 2.0
		t	6.5 – 9.0	9.5 – 10.5
C	Present state (quenched)	z	0 – 0.3	0 – 0.3
		t	0 – 3.5	0 – 3.5

contributions of particles along the line of sight (LoS), smoothed by the Wendland-C2 kernel W (Wendland 1995) implemented in SWIFTSIMIO (Borrow & Borrisov 2020). Thus, the contributions of the jth particle to the ith pixel is computed as

$$R_i = \frac{\sum_{j\,\in\,\mathrm{LoS}} m_{i,\mathrm{hot}}\, W_{i,j}(h_j)}{\sum_{j\,\in\,\mathrm{LoS}} m_{i,\mathrm{cold}}\, W_{i,j}(h_j)}, \tag{15}$$

where $m_{i,\mathrm{hot}}$ are the gas particle masses with temperature $T \geq 10^5$ K, $m_{i,\mathrm{cold}}$ those with $T < 10^5$ K, and h_j is the SPH smoothing length of the jth particle. The ratio in equation (15) is shortened to $\sum_{\mathrm{hot}} m_i / \sum_{\mathrm{cold}} m_i$ in Fig. 2. The maps show the projected mass ratio with blue shades indicating an LoS with more cold gas than hot, and red shades indicating the opposite. In the centre, areas without any cold gas along the LoS are shown in grey.

The two A→B→C map sequences show the evolution of the group and cluster's IGM from being mainly cold (phase A), to having similar hot and cold gas fractions during merger events (phase B, the second row of Fig. 3), and finally to a hot-gas phase (C). For the projected mass ratio in the latter phase, we overlay the map of the hot gas mass (in grey shades) to render the underlying diffuse hot gas distribution within and around r_{500}. All quantities are given in the physical reference frame at the corresponding redshift.

The maps in columns 2–3 and 4–5 show the emission-measure-weighted (EMW) temperature and the MW entropy, respectively; each pair breaks down the IGM gas into the cold (2 and 4), and hot (3 and 5) phases. The EMW temperature for the i^{th} pixel is defined as

$$T_{i,\mathrm{emw}} = \sum_{j\,\in\,\mathrm{LoS}} m_i \rho_i\, T_i\, W_{i,j}(h_j) \Big/ \sum_{j\,\in\,\mathrm{LoS}} m_i \rho_i\, W_{i,j}(h_j), \tag{16}$$

where the emission measure is $\propto m_i \rho_i$ and ρ is the SPH gas density. The MW entropy is defined similarly but without the ρ-weights:

$$K_{i,\mathrm{mw}} = \sum_{j\,\in\,\mathrm{LoS}} m_i\, K_i\, W_{i,j}(h_j) \Big/ \sum_{j\,\in\,\mathrm{LoS}} m_i\, W_{i,j}(h_j), \tag{17}$$

with $K_i = k_{\mathrm{B}} T_i / n_{e,i}^{2/3}$. Most IGM gas is cold in phase A and starts with temperatures and entropies lower than the self-similar values. During phase B, when the to-be group has the size of a galaxy and the to-be cluster has the size of a group, the amount of hot gas increases in the central region and cold, low-entropy gas streams form in the surroundings. By $z = 0$ (phase C), hardly any cold gas can be found within r_{500}; the entropy maps show a uniform distribution on scales of $\approx r_{500}$ for the group and scales of $\approx 0.3\, r_{500}$ for the cluster, as Paper I found previously.

4.3 Baryon content

The baryon, gas, and star fractions are displayed in Fig. 3 with the same layout as in Fig. 1. First, we define these additional metrics and then describe the main features of their evolutionary profiles.

The gas mass M_{gas} is computed by summing the mass of all gas particles within r_{500}. M_{gas} is equivalent to the sum of the hot gas mass $M_{\mathrm{gas,hot}}$, which accounts for gas above 10^5 K, and the cold gas mass $M_{\mathrm{gas,cold}}$, which accounts for gas below 10^5 K. The hot and cold gas fractions are obtained by dividing their respective masses by M_{500}. In the middle row of Fig. 3, the gas fraction $f_{\mathrm{gas}} = M_{\mathrm{gas}}/M_{500}$ is split into hot (solid lines) and cold (dotted lines). The stellar mass $M_\star$ is the sum of the mass of all stellar particles inside r_{500}. From this definition, the star fraction is expressed as $f_\star = M_\star/M_{500}$. Finally, the baryon fraction is the sum of the gas and star fractions: $f_{\mathrm{gas}} + f_\star \equiv (M_{\mathrm{gas}} + M_\star)/M_{500}$. In the top row of Fig. 3, the solid lines show the baryon fraction including all gas (hot and cold), while the dotted lines exclude cold gas.

Focusing on the top row of Fig. 3, the (total) baryon fraction of both objects starts close to the Universal value of $f_{\mathrm{bary}} = 0.157$ (Planck Collaboration VI 2020) at $z \approx 10$. This result is consistent with little SN and AGN feedback at such early times (see also the BHMAR in Fig. 1). However, the late-time evolution for $z < 2$ shows the outcomes of two competing effects: the deepening of the gravitational potential well (hence accretion) and the intensified feedback activity. In the group, the total baryon fraction gradually decreases because of the gas ejected by feedback. On the other hand, the cluster's gravitational potential is strong enough to hold onto the gas despite the feedback, causing an increase in the total baryon fraction. This result indicates that feedback has a stronger effect on groups than in clusters, in line with previous numerical (McCarthy et al. 2010, 2011; Gaspari et al. 2011) and observational (Akino et al. 2022; Poon et al. 2023) studies, and physical intuition.

The impact of AGN feedback on the IGM raises the question of whether a different variation of the feedback model could lead to a net loss of baryons for the cluster too. In our previous investigation of this particular cluster (Paper I), we did not find evidence that a different feedback energy-injection scheme or moderately more explosive AGN feedback could have ejected more baryons in the form of hot gas. Tests with a higher AGN heating temperature ($\Delta T_{\mathrm{AGN}} = 10^9$ K) have shown little impact on the baryon fraction at $z = 0$. However, increasing ΔT_{AGN} did lead to higher entropy levels in the core, thereby exacerbating the core entropy excess relative to the self-similar expectation. The total time-integrated energy available for AGN feedback was kept constant in these experiments.

From early times until the beginning of phase A, cold gas is the primary component of the baryon content in both systems: the cold gas fractions are high, $f_{\mathrm{gas,cold}} \approx 0.1$ and the hot gas fractions are low, $f_{\mathrm{gas,hot}} \approx 0.01$. This is also reflected in the baryon fraction with and without cold gas (top row of Fig. 3). During this phase, the central BHs have not started their non-linear growth phase yet, and the AGN activity remain low. However, by $z \approx 4$, the sSFR begins to decrease, suggesting that the abundant cold gas feeds star formation, and SN feedback regulates the IGM thermodynamics in haloes of mass scales $\sim 10^{12}$ M$_\odot$, i.e. small galaxies. This result is consistent with the equilibrium mechanisms modelled in Dekel & Mandelker (2014).

When the halo mass reaches $\sim 10^{12}$ M$_\odot$ (galaxy scale, phase A), the gas heats up, and the SN feedback is no longer effective (e.g. Bower et al. 2017). Instead, the gas can now efficiently feed the cSMBH and the BHMAR reaches its peak, which clearly coincides with the decrease of $f_{\mathrm{gas,cold}}$ below $f_{\mathrm{gas,hot}}$ in Fig. 3 (middle row). By

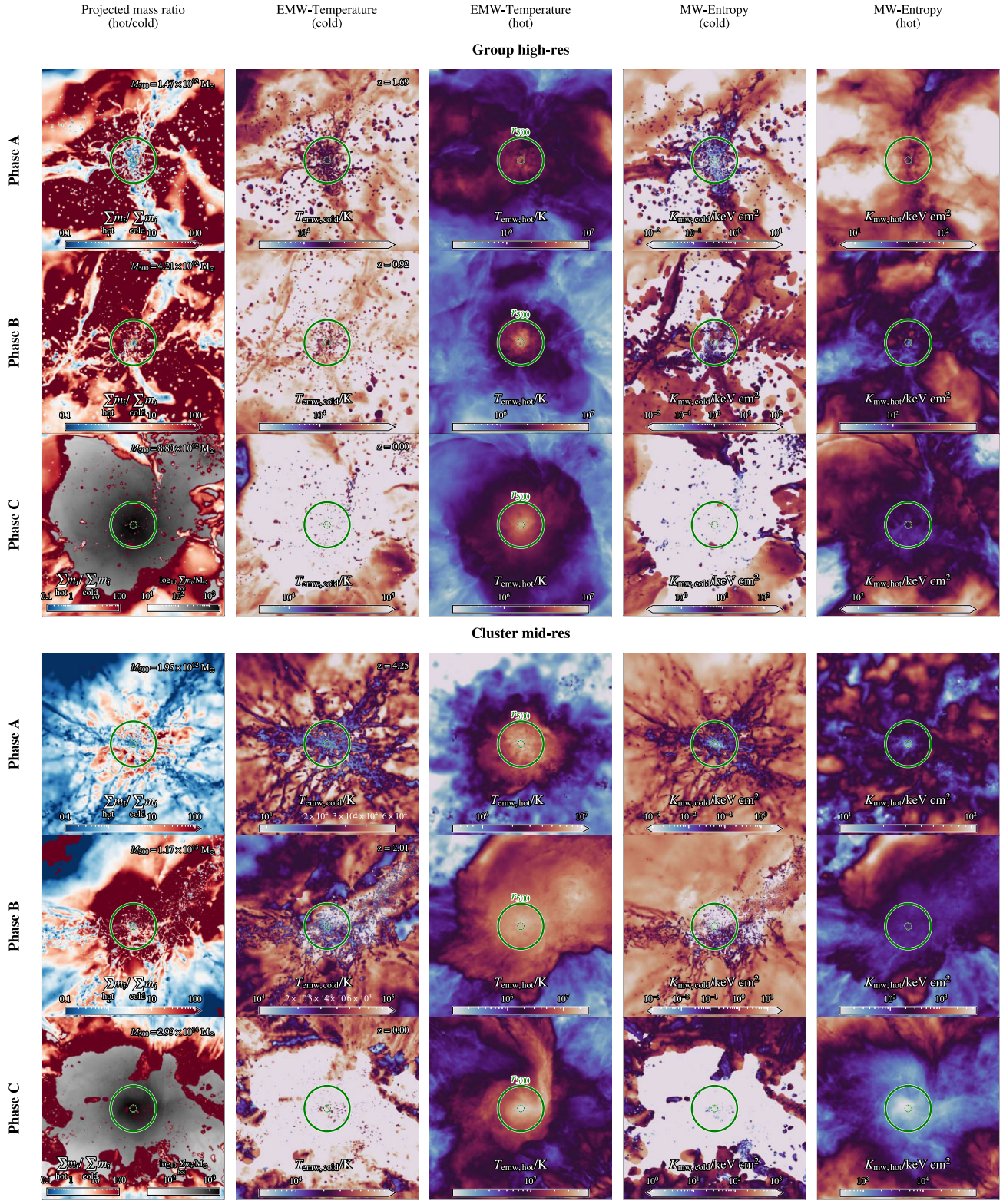

Figure 2. Projected maps of the group (top three rows) and the cluster (bottom three rows), run with the Ref model at high- and mid-res, respectively. From top to bottom, the rows correspond to phase A (quasar mode), B (merger), and C (quenched). The five columns show the following projected quantities, from left to right: (i) ratio of the projected hot gas mass to projected cold gas mass, as defined in equation (15); (ii) the EMW temperature of the cold gas, followed by (iii) the same but for hot gas; finally, (iv) the MW projected entropy of the cold gas, and (v) the same but for hot gas. The projected mass ratio is masked in solid red where all gas is hot; white areas indicate no particles matching the temperature selection in other maps. For phase C, we overlay the projected mass ratio without cold gas (in grey) with the map of the hot gas to visualize the underlying gas distribution. The projections along the z-axis are constructed from a spatial cube of (physical) volume $(4\,r_{500})^3$ around the centre of the objects. r_{500} and the core radius, $0.15\,r_{500}$, are indicated by green solid and dashed circles, respectively.

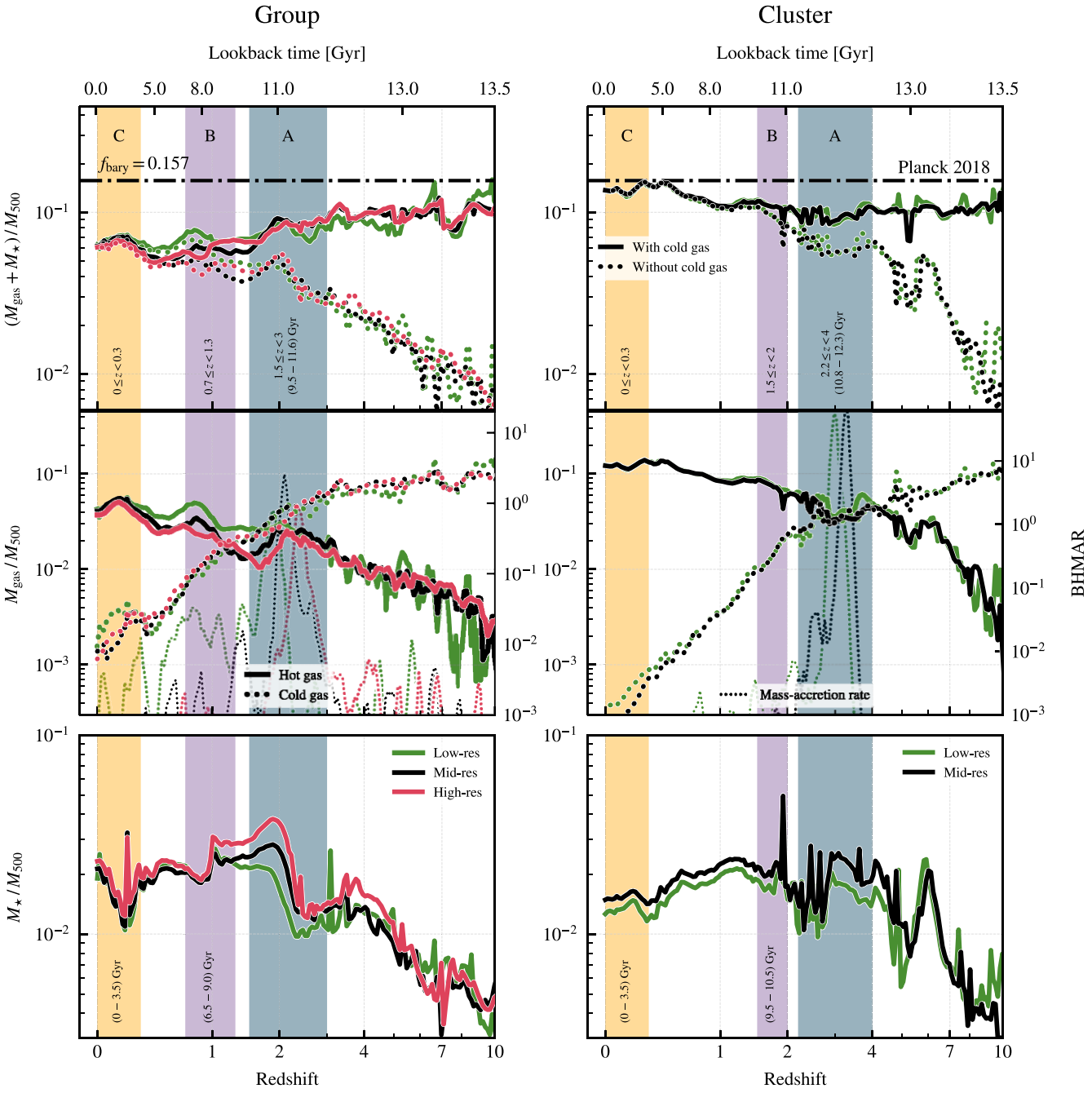

Figure 3. From top to bottom, we show the redshift/time evolution of the baryon fraction $[(M_{\rm gas} + M_\star)/M_{500}]$, the hot gas fraction $(M_{\rm gas}/M_{500})$, the star fraction $(M_\star/M_{500})$, and the BCG mass fraction $(M_{\rm BCG}/M_\star)$ within r_{500}. In the top panels, solid lines indicate the baryon fraction accounting for all gas (cold and hot), while the dotted lines only include hot gas. The dash–dotted line shows the Universal baryon fraction $f_{\rm bary} = 0.157$ for the *Planck* 2018 cosmology (Planck Collaboration VI 2020). In the middle panels, the solid lines show the fraction of hot gas and the (thick) dotted lines show the fraction of cold gas; and the thin dotted lines represent the BHMAR. The stellar component of the BCG is defined by a spherical aperture with a fixed physical radius of 50 kpc. The x-axes and the layout are as in Fig. 1.

the end of phase B, the cSMBH grows further and AGN feedback becomes the main process regulating the IGM thermodynamics and shutting down star formation. We find this effect in both objects; however, it is most apparent in the group, where a significant dip in sSFR happens earlier. Moreover, the cSMBH appears to reach the peak of its growth rate when the halo has mass $\approx 10^{12}$ $M_\odot$, independent of the redshift, in agreement with the original EAGLE simulations (see fig. 6 of Bower et al. 2017). Also in line with the same study, the cSMBHs hosted by our simulated haloes have slowed down their growth rate by the end of the merger phase, once the system surpassed the 'transition mass'.

The resulting IGM state (phase C) features quenched BCGs and small cold gas fractions. For both objects, we find that higher resolution simulations produce more stars, except for the low-res group at low redshift with a nearly converged $f_\star$. This feature can be observed in most phases of the $f_\star$ evolution and is in line with fig. 5 of Paper I.

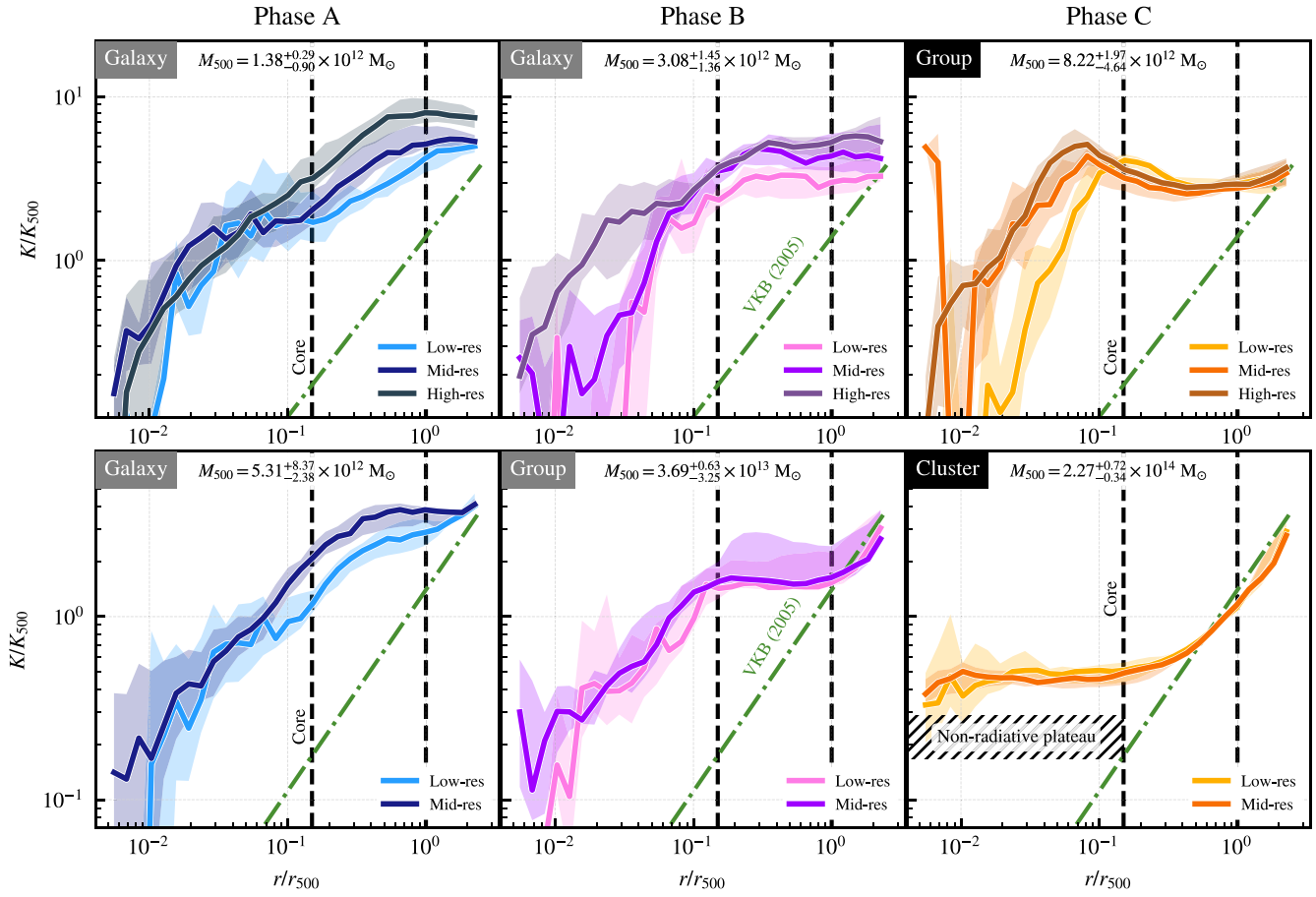

Figure 4. Scaled entropy profiles for the group (top) and the cluster (bottom) during the three evolutionary phases in Table 2. The grey labels indicate the mass scale of the halo in each phase, and the black labels indicate the $z = 0$ mass scale of the objects. The solid lines represent the median entropy profiles in the respective redshift interval, and the shaded region is the first and third quartile levels. From left to right: Phase A covers the high-redshift (quasar-mode) evolution, Phase B the intermediate redshift during mergers, and Phase C captures the low-redshift thermodynamic state ($z < 0.3$). The colour coding for the three phases is the same as in Fig. 1. In each panel, the runs at different resolutions are shown with varying saturation and luminance in the same colour-space region. For the group, we show the low-, mid-, and high-res entropy profiles, while for the cluster we only include the low- and mid-res profiles. The profiles are plotted out to $2.5\,r_{500}$. The green dash–dotted line is the self-similar NR entropy baseline (VKB, Voit et al. 2005), and the vertical dashed lines are guidelines for the core radius ($0.15\,r_{500}$, as indicated) and r_{500}. The M_{500} mass, laid out as $(\text{median})^{+(\text{max}-\text{median})}_{-(\text{median}-\text{min})}$ for each phase is shown at the top of each panel. The hatched region in the cluster's entropy profiles indicates the entropy level of the plateau in the core of the corresponding NR simulations (see Appendix A). Here, the Ref level is higher than in NR, indicating a clear entropy excess.

4.4 Entropy profiles

Now, we study the entropy profiles of the objects during each of the three evolutionary phases defined in Section 4.1. For each phase, we compute the median profile, together with the first and third quartiles. In NR conditions, the group and cluster develop clear power-law-like entropy profiles, behaving as expected. These profiles are reported in Appendix A. For the Ref model, we present the group and cluster profiles in Fig. 4. To compute the entropy, we only include the highly ionized gas in the X-ray-emitting phase, defined by the temperature cut $T > 10^5$ K. The entropy profiles are shown down to 1 per cent of r_{500}. In addition, we truncate the entropy profiles where the number of particles within the spherical shell falls below 50 if this radius is larger than $0.01\,r_{500}$.

In Fig. 4, the group entropy profiles are on the top row, while the cluster profiles are on the bottom row. The panels are arranged in three columns, with the respective evolutionary phase indicated at the top. In each panel, we show the entropy profiles at different resolutions for a given object during a fixed redshift interval. The solid lines show the median profiles, and the bands represent the extent between the first and third quartiles. Darker colours correspond to higher resolution and lighter colours to lower resolution. We outline two key features of these results: the shape of the profiles and the dependence on resolution.

Next, we track the evolution of the logarithmic gradient of the entropy profile, defined as

$$\alpha_K = \frac{\mathrm{d}\log(K)}{\mathrm{d}\log(r)} = \frac{\mathrm{d}\log(K/K_{500})}{\mathrm{d}\log(r/r_{500})}. \tag{18}$$

We sample the average local gradient $\langle\alpha_K\rangle$ in two radial regions: the core, $0.05 \leq r/r_{500} < 0.15$, and the outskirts, $0.5 \leq r/r_{500} < 2$. The slope is obtained from a least-squares linear fit of the entropy profile in logarithmic space, using the data in the corresponding radial range. The two slopes, labelled $\langle\alpha_{K,\text{core}}\rangle$ and $\langle\alpha_{K,\text{outskirts}}\rangle$, are computed for each redshift snapshot and plotted as a function of the scaled halo mass $M_{500}(z)/M_{500}(z=0)$ in Fig. 5. Normalizing $M_{500}(z)$ by its present-day value shows the group and cluster's growth within the same x-axis range and, hence, facilitates the comparison of the $\langle\alpha_K\rangle$ evolution. In the plot, filled markers represent $\langle\alpha_{K,\text{core}}\rangle$ and

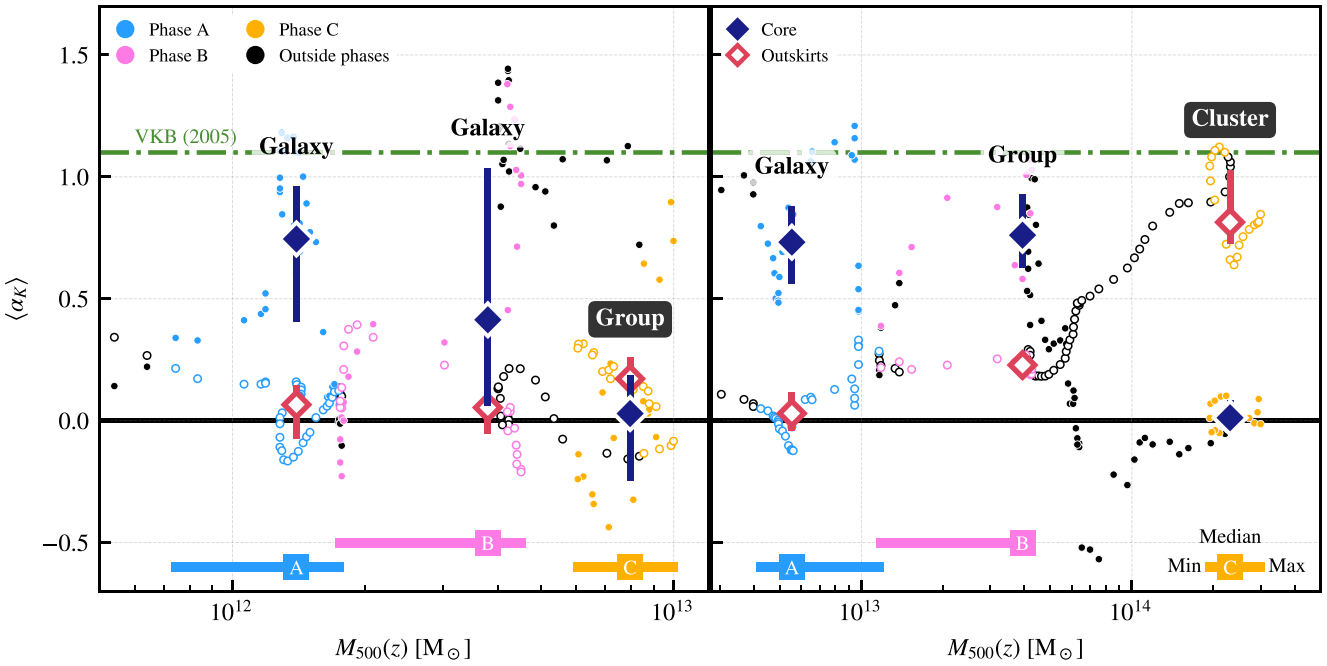

Figure 5. Evolution of the logarithmic gradient of the entropy profile α_K with halo growth, parametrized as $M_{500}(z)$, for the group at high-res (left) and the cluster at mid-res (right). The average gradient $\langle\alpha_K\rangle$ in the core is shown as filled markers and for the outskirts as empty markers. The small circles, one per simulation snapshot, are coloured in blue, pink, and yellow, corresponding to the evolutionary phases A, B, and C, respectively. Snapshots recorded outside the redshift bounds of the phases are shown in black. For each phase, the larger diamond markers show the median gradient and the first and third quartiles. The dash–dotted line is the gradient of the NR gravitational baseline (VKB, Voit et al. 2005), as in Fig. 4. At the bottom, the squares indicate each phase's median, minimum and maximum fractional halo mass. Note that the group experiences a small decrease in M_{500} at the end of phase C, resulting in x-values slightly above $M_{500}(z = 0)$.

empty markers $\langle\alpha_{K,\mathrm{outskirts}}\rangle$; these are coloured by the corresponding evolutionary phase, or in black if the snapshot's redshift does not correspond a particular phase. To better visualize the evolution of $\langle\alpha_K\rangle$ with noisy single-snapshot data, we smoothed the values by computing a moving average over seven adjacent snapshots in phase A, 3 in B, and 2 in C. The diminishing levels of smoothing are required by the higher statistical noise in the profiles at high redshift than at low redshift, especially in the core region.

4.4.1 *Profile shape and gradient at different mass scales*

During phase A, the to-be group is hosted by a galaxy-sized halo with M_{500} just above 10^{12} M$_\odot$. The entropy profile is clearly power-law-like between r_{500} and the core radius ($0.15\,r_{500}$). The entropy at r_{500}, $K(r = r_{500})$, is around an order of magnitude higher than the self-similar gravitational baseline shown in green (VKB, Voit et al. 2005), suggesting a departure from self-similarity which was also found in other simulations of galaxy-sized objects (e.g. Gaspari et al. 2014).

As the halo grows into a (larger) galaxy-sized one through mergers ($M_{500} \approx 3 \times 10^{12}$ M$_\odot$, phase B), the entropy profile flattens at the virial radius; however, the core entropy remains largely unchanged relative to K_{500}. Interestingly, a similar shape appears in the profile of the other galaxy (to-be cluster) at $M_{500} \approx 5 \times 10^{12}$ M$_\odot$ in phase A. The logarithmic entropy gradient in the two galaxies' cores and outskirts confirms this result. In Fig. 5, we compare the 'galaxy' α_K values in the left and the right panels, corresponding to phases B and A, respectively. In the outskirts, we find $\alpha_K \approx 0$ in both cases; in the core, the α_K values are also within the first and third quartile levels, despite the left panel showing more variability. Examining the latter case closely, the scatter is large because phase B includes $\alpha_{K,\mathrm{core}}$ samples with low values at the beginning, before the merger, and high values towards the end, after the merger, when the halo grows to the size of a large galaxy. This consideration indicates that the high $\alpha_{K,\mathrm{core}}$ values should be considered when comparing to the galaxy in the right panel, thus strengthening the similarity.

The two galaxy-sized objects show that the entropy profile at the virial radius becomes flat regardless of a merger event happening: when the halo mass reaches $3 - 5 \times 10^{12}$ M$_\odot$, the group series already recorded a merger event in phase B, but the cluster series, in phase A, has not.

On group scales ($0.8 - 4 \times 10^{13}$ M$_\odot$ for our objects), the entropy profile is the flattest at r_{500}, but in the centre we still find a power law. Finally, on cluster scales ($\approx 2 \times 10^{14}$ M$_\odot$), the gravitational power-law profile emerges at large radii, while the profile in the core flattens to a level ≈ 0.2 dex above the NR plateau.

In summary, Figs 5 and 4 show that the entropy plateau appears to emerge (i) at the virial radius when the halo reaches a characteristic mass scale of $\sim 10^{12}$ M$_\odot$ and (ii) in the core at cluster scales. Since this characteristic mass scale is similar to that of the transition from SN- to AGN-feedback-driven self-regulation of the IGM (Bower et al. 2017), it is natural to ask whether the plateau emerges due to processes occurring before AGN feedback or around the same time as AGN activity starts.

By definition, both objects record the peak in SMBH activity in phase A. During this time, the to-be cluster also reaches a state of 'cold–hot gas equality' ($f_{\mathrm{gas,cold}} \approx f_{\mathrm{gas,hot}}$, see Fig. 3) at the characteristic mass. However, in the to-be group, this occurs with a delay: the state with $f_{\mathrm{gas,cold}} \approx f_{\mathrm{gas,hot}}$ at the characteristic mass is recorded during phase B when the entropy distribution at the virial

radius is flattened. Therefore, the formation of the plateau at large radii in group-mass haloes appears to be due to processes that become important when the IGM becomes dominated by hot gas.

4.4.2 *Numerical convergence*

Overall, most metrics tracked in Figs 1 and 3 show good numerical convergence at the three resolutions. On the other hand, the numerical resolution has a small impact on the scaled entropy profiles of the group in Fig. 4. In phase A, high-res simulations produced entropy levels that are 0.3 dex higher than mid-res between the core and the virial radius. In phases B and C, the high-res profiles are higher in the core, while the entropy outside the core is well converged. This effect is due to the removal of hot gas that cools to form stars. We find that star formation is enhanced in the high-res group compared to the low- and mid-res simulations, as shown in the bottom-left panel of Fig. 3.

Even in the group's case, the discrepancy between resolutions is small and does not affect our results qualitatively.

5 LAGRANGIAN PARTICLE HISTORIES

One compelling hypothesis for the excess entropy, relative to the self-similar expectation, observed in our simulated objects is the hot gas ejection scenario. In this picture, initially cold gas is heated directly by SN feedback (before phase A) and then by AGNs. As its temperature increases, the gas is ejected from the halo, leaving behind a higher entropy medium. To test this hypothesis, we match individual gas particles between our Ref and NR simulations following the procedure outlined in McCarthy et al. (2011, see Section 3.2). This matching allows us to directly compare the thermodynamic histories of identical particles under different physical assumptions.

Figs 6 and 7 illustrate the median Lagrangian histories of key thermodynamic quantities for gas particles in the group and the cluster, respectively, at mid-res. In each figure, the rows (from top to bottom) show the evolution of the (median) scaled distance from the potential minimum $r/r_{500}(z)$, entropy $K/K_{500}(z=0)$, temperature $T/T_{500}(z=0)$, and density $\rho/\rho_{\rm mean}(z)$. Here, the self-similar values are computed at $z=0$; the density and radial distance are normalized to the mean density of the universe, $\rho_{\rm mean}(z)=\Omega_{\rm m}\,\rho_{\rm crit}(z)$, and $r_{500}(z)$, respectively.

The panels are arranged by the region in which the gas is located at $z=0$: the core ($r<0.15\,r_{500}$, left column), the intermediate intra-group/-cluster region ($0.15<r/r_{500}<1$, centre), and the outskirts ($1<r/r_{500}<6$, right).

Each panel distinguishes gas samples using a consistent colour and line code:

(i) *Red solid*. Gas particles selected in Ref that end up hot and inside the region at $z=0$, tracked in the Ref simulation. From Section 3.2, this particle subset is defined as $\mathrm{Ref}(z>0)\in\mathrm{Ref}(z=0)$.

(ii) *Blue solid:* Gas particles selected in NR that end up inside the region in NR at $z=0$ tracked in NR: $\mathrm{NR}(z>0)\in\mathrm{NR}(z=0)$.

(iii) *Red dashed.* The same NR-selected particles, but tracked in the Ref simulation (restricted to gas particles that are not converted into stars or have cooled below the star formation threshold). This selection is defined by $\mathrm{Ref}(z>0)\in\mathrm{NR}(z=0)$.

(iv) *Blue dashed:* Gas particles selected in Ref that end up hot and inside the region at $z=0$, tracked in the NR simulation: $\mathrm{NR}(z>0)\in\mathrm{Ref}(z=0)$. This sample addresses the question 'what would the history of the Ref-selected gas have been in the absence of feedback or radiative cooling?'

Let us first consider the evolution of gas particles in the group, the system with the largest entropy excess as seen in Fig. 4. The key plots to focus on are the halocentric distance, $r_{\rm CoP}$ (first row), and the entropy, K (second row).

Comparing the NR-selected gas ($\mathrm{NR}(z>0)\in\mathrm{NR}(z=0)$, blue solid) with the same gas tracked in Ref ($\mathrm{Ref}(z>0)\in\mathrm{NR}(z=0)$, red dashed), we find that the latter remains at several core radii away from the centre of potential. The two histories begin to diverge between $z=2$ and 1 as a consequence of feedback processes active at high z. The same curves in the entropy and temperature panels (second and third rows) show that this ejected gas has indeed been heated and remains at large radii, avoiding cooling down and forming stars. Moreover, the red dashed entropy is much higher than the blue solid due to their density (bottom row) being much lower; hence, the gas accreting process must be very different in Ref than in NR.

The blue dashed sample ($\mathrm{NR}(z>0)\in\mathrm{Ref}(z=0)$) has, for the most part, higher entropy than the blue solid ($\mathrm{NR}(z>0)\in\mathrm{NR}(z=0)$), which was selected in NR. Hence, the gas that replaces the ejected gas in Ref already had higher entropy initially in NR, so that the final entropy distribution of the gas in Ref is a mixture of the initial selection (the gas required to replace the ejecta), and the sample whose entropy changed as a result of losing gas from cooling and star formation in Ref, possibly causing the red solid ($\mathrm{Ref}(z>0)\in\mathrm{Ref}(z=0)$) and blue dashed lines not to overlap perfectly. We note that comparing blue solid with red dashed ($\mathrm{Ref}(z>0)\in\mathrm{NR}(z=0)$) is not straightforward, since the red dashed line represents a sample of gas particles that survived as hot gas until $z=0$ in Ref, as previously highlighted. Therefore, the red dashed sample may reflect a biased subset in NR upon matching particles. While this result is robust and useful to understand the Lagrangian entropy history, future work should further characterize the impact of this bias on the thermodynamic properties of the particle ensembles.

Now, we assess the red solid ($\mathrm{Ref}(z>0)\in\mathrm{Ref}(z=0)$) and blue dashed ($\mathrm{NR}(z>0)\in\mathrm{Ref}(z=0)$) samples; this comparison is cleaner compared to the previous one, because all the gas particles in Ref at $z=0$ can be located in NR. The Ref-selected gas ($\mathrm{Ref}(z>0)\in\mathrm{Ref}(z=0)$, red solid) which ends up in the group's core ($r<0.15\,r_{500}$), is outside the halo in NR (blue dashed) at $z=0$. The red solid and blue dashed samples have comparable median entropy despite the gas particles being located at different radii, thus proving that the hot halo gas in NR was ejected, and the Ref gas is new material that replaced it. By contrast, the difference between the blue solid and red dashed ($\mathrm{Ref}(z>0)\in\mathrm{NR}(z=0)$) curves is much greater than between the red solid and blue dashed, suggesting that the gas that has taken the place of the ejected material has not been heated as much as the ejected gas itself. In summary, much of the excess entropy in the Ref group does originate from the movement of particles to replace those that have cooled or were ejected. Upon closer inspection, the entropy of the Ref-selected gas is slightly higher than that of the NR-selected gas ($\mathrm{NR}(z>0)\in\mathrm{NR}(z=0)$, blue solid), suggesting an entropy excess for the Ref hot gas that does at least partly originate from the selection of the particles.

We also note that the entropy histories of the red solid ($\mathrm{Ref}(z>0)\in\mathrm{Ref}(z=0)$) and blue dashed ($\mathrm{NR}(z>0)\in\mathrm{Ref}(z=0)$) samples differ at $z>0.3$, with the blue dashed line increasing faster than the red solid. On the other hand, these samples have very similar histories in terms of temperature and halocentric distance (for $z>0.3$), implying that the entropy excess is induced by a deficit in density, as shown in the third row. Near $z=0$, the self-similarly scaled temperature, density, and entropy of the Ref-tracked particles (red solid) increase, while they remain roughly constant (or show an inverse trend) for the NR-tracked sample (blue dashed).

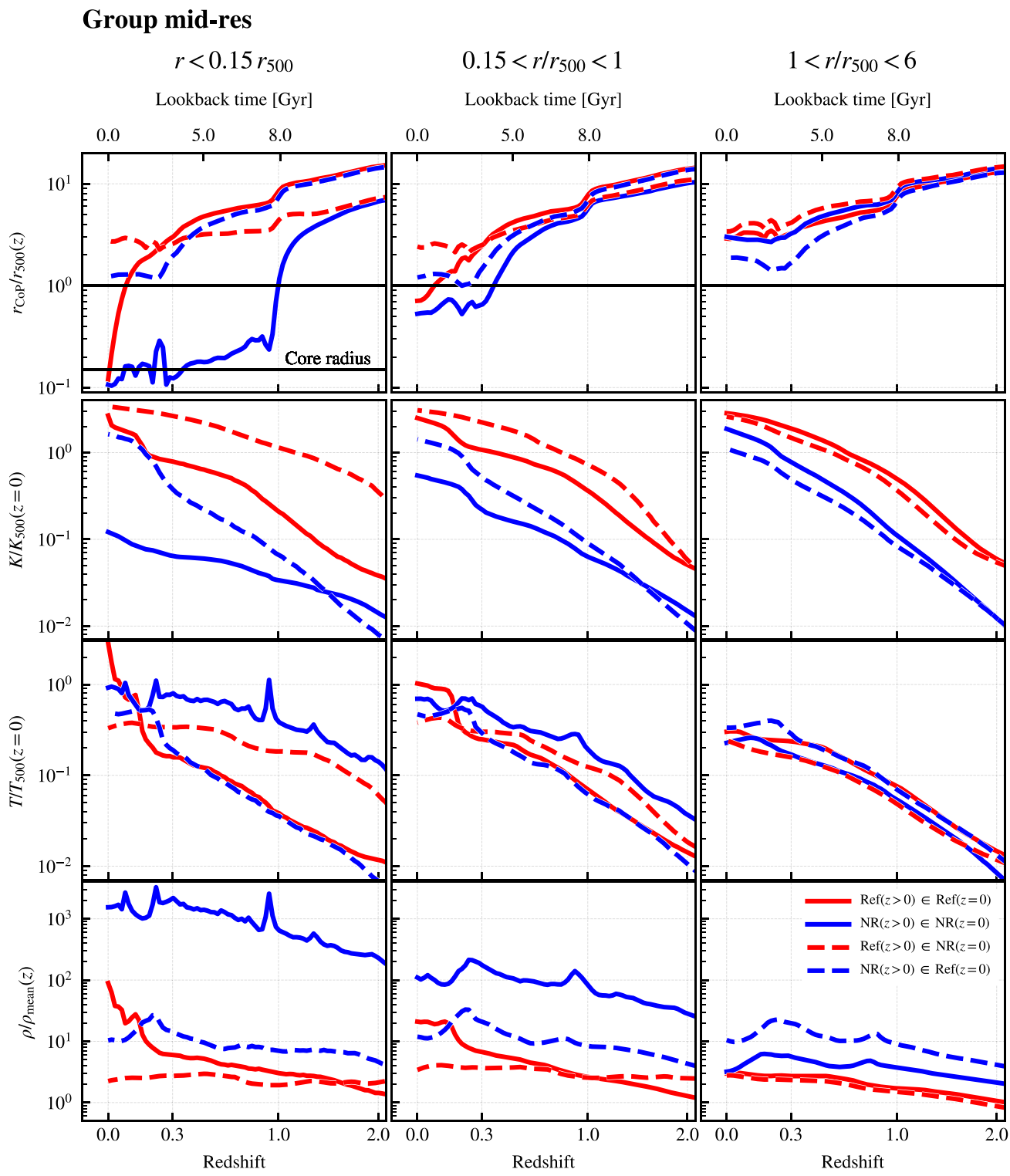

Figure 6. From top to bottom: Lagrangian history of the median scaled halocentric distance ($r_{\rm CoP}$), entropy (K), temperature (T), and density (ρ) of gas particles in the group at mid-res. From left to right: the particles are identified in three spherical regions defined at $z = 0$: the core ($r < 0.15\,r_{500}$, left), the rest of the intragroup medium ($0.15 < r/r_{500} < 1$, centre), and outside r_{500} (right), as indicated at the top of the panels. These radii are also indicated in the overview maps of Fig. 2. The particles in each spherical region are selected in three ways: (i) gas particles in Ref that end up hot and inside the region in Ref at $z = 0$ (red solid); (ii) gas particles in NR that end up inside the region in NR at $z = 0$ (solid blue); (iii) gas particles in NR that end up in the region in Ref at $z = 0$ (dashed blue); and (iv) gas particles in Ref that end up in the region in NR at $z = 0$ (dashed red). The entropy and temperatures are normalized to the self-similar value at $z = 0$; the density is normalized to the mean matter density at each redshift, $\rho_{\rm mean}(z) = \Omega_{\rm m}\,\rho_{\rm crit}(z)$; the radius is normalized to $r_{500}(z)$ and computed at each redshift. The horizontal black lines indicate r_{500} and the core radius, $0.15\,r_{500}$.

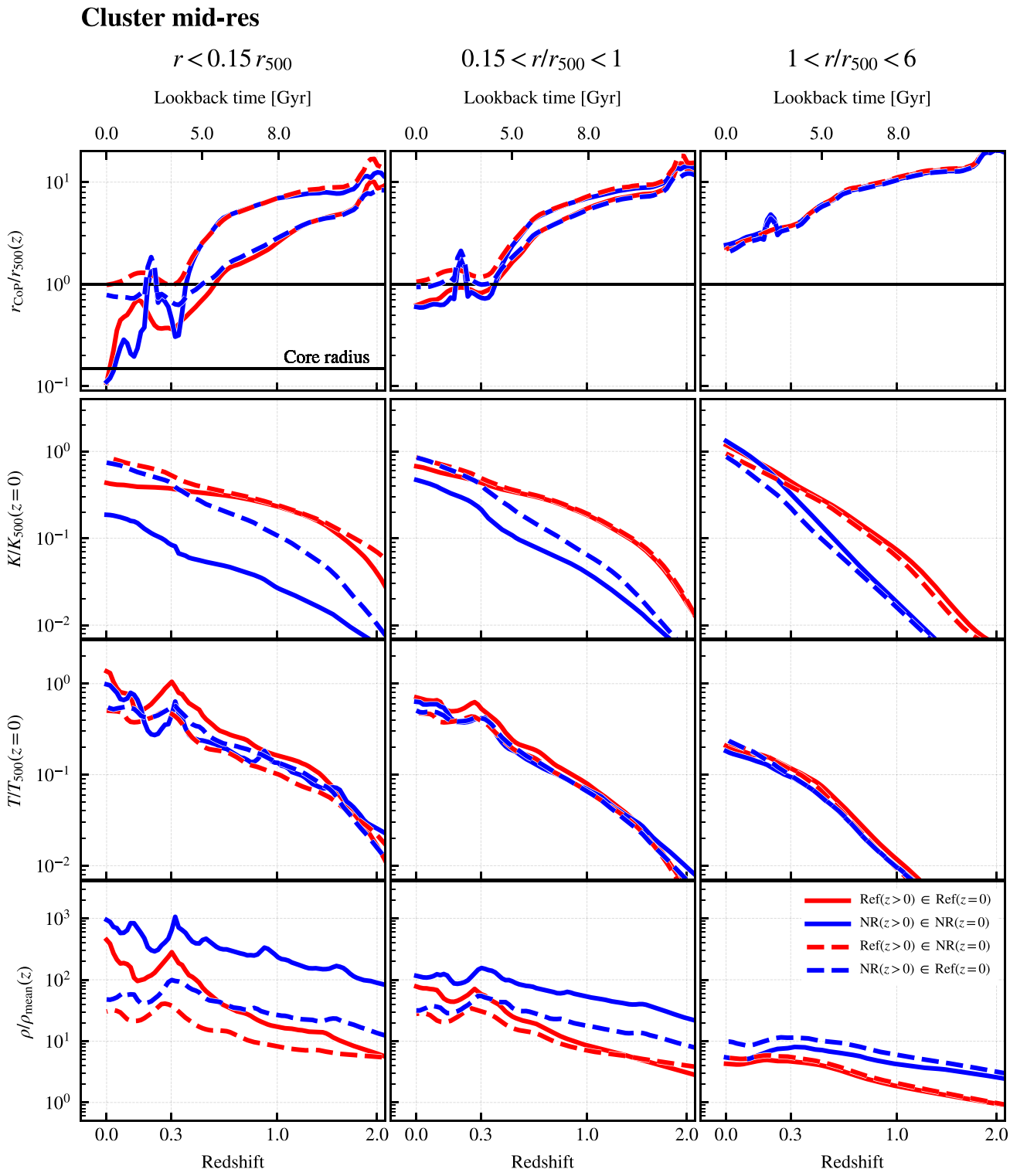

Figure 7. As in Fig. 6, but for the cluster at mid-res.

This result, together with a rapidly decreasing halocentric distance, suggests that radiative cooling in Ref drives a cooling flow which increases the gas density, and causes it to fall into the potential well. Once in the core (horizontal line), the gas compresses and undergoes shock-heating. A trace of this process can be observed in the $z = 0$ projected-mass-ratio map in Fig. 2, where a filament in the outskirts of the group is captured before sinking and collapsing.

In the intermediate shell ($0.15 < r/r_{500} < 1$) – where the entropy plateau is most prominent – the thermodynamic evolution (T, ρ, K) is similar to the core. At $z > 0.3$, the entropy excess between the red solid and blue dashed samples is larger than the present day.

In the outskirts of the group ($1 < r/r_{500} < 6$), the median histories of NR-tracked particles selected in NR (NR($z > 0$) $\in$ NR($z = 0$), blue solid) and Ref (NR($z > 0$) $\in$ Ref($z = 0$), blue dashed) are very similar. This indicates that, in these regions, the thermodynamic evolution is largely insensitive to where the particles end up or how hot they become as a consequence of the subgrid physics.

The cluster plots in Fig. 7 exhibit trends similar to those in the group, with notable differences. In the core region, the entropy histories of Ref-selected particles in NR (NR($z > 0$) $\in$ Ref($z = 0$), blue dashed) and Ref (Ref($z > 0$) $\in$ Ref($z = 0$), red solid) differ at higher redshifts, indicating the presence of feedback activity, consistent with McCarthy et al. (2011). Temperature and density histories also reflect these trends, with radiative cooling in Ref driving cooling flows that increase gas density (the red solid $\rho(z = 0)$ is higher than the blue dashed). In the cluster, unlike the group, the entropy plateau is most manifest in the core; however, the entropy histories in the intermediate region are similar to those in the core. The outskirts show nearly identical median histories for NR-tracked particles selected in NR (NR($z > 0$) $\in$ NR($z = 0$), blue solid) and Ref (NR($z > 0$) $\in$ Ref($z = 0$), blue dashed), indicating that thermodynamic evolution in these regions is largely unaffected by subgrid physics. These observations also align with McCarthy et al. (2011), highlighting the scale-dependent impact of feedback on the entropy and thermal evolution of the IGM. Given these considerations, a key result is that the entropy and halocentric radius of the blue dashed line (NR($z > 0$) $\in$ Ref($z = 0$)) end up above the red line (Ref($z > 0$) $\in$ Ref($z = 0$)) in the region of the entropy core. This behaviour suggests that the core entropy in Ref is high because the hot gas in NR also has high entropy. Therefore, the core-entropy excess in Ref cannot directly be due to AGN feedback, also because the gas sinks to smaller radii instead of being directly heated and buoyantly moving outwards. Secondary feedback-induced shocks could nevertheless have an impact (Vazza 2011).

6 DISCUSSION AND CONCLUSIONS

We carried out cosmological zoom-in simulations of a galaxy group of mass $M_{500} = 8.83 \times 10^{12}$ M$_\odot$ and a galaxy cluster of mass $M_{500} = 2.92 \times 10^{14}$ M$_\odot$ at $z = 0$ using the SWIFT-EAGLE reference model. In our mid-resolution runs (matching the resolution of the EAGLE L100N1504 volume of Schaye et al. 2015) dark-matter particles have mass $m_{\rm DM} = 9.82 \times 10^6$ M$_\odot$ and gas particles $m_{\rm gas} = 1.83 \times 10^6$ M$_\odot$; low-resolution simulations have particle masses eight times larger; and the high-resolution simulation of the group uses $m_{\rm DM} = 1.23 \times 10^6$ M$_\odot$ and $m_{\rm gas} = 2.29 \times 10^5$ M$_\odot$. Our study investigates the entropy evolution of groups and clusters of galaxies, extending our previous research on the entropy excess relative to the self-similar expectation in Altamura et al. (2023) to higher redshifts. In light of recent X-ray observations (Eckert et al. 2024), the entropy-core problem highlighted in our previous work appears to have emerged due to an observational selection bias [effects on averaged thermodynamic profiles and hot gas fractions are discussed in Clerc et al. (2024) and Popesso et al. (2024), respectively]. By analysing the thermodynamic history of the IGM, we identified three key moments in the evolution of these systems that we link to their entropy structure.

A key result is that entropy plateaus appear to emerge at characteristic halo masses and that their formation is closely linked to AGN feedback: when a system reaches $\sim 10^{12}$ M$_\odot$, its entropy profile flattens at the virial radius (Fig. 4, left column). This transition corresponds to the point where AGN feedback dominates the thermodynamic regulation, as evidenced by the peak in the specific BH accretion rate (Fig. 1, bottom row). In groups ($\sim 10^{13}$ M$_\odot$), this plateau extends down to the core-radius, forming a broad region of nearly constant entropy, and at cluster scales ($\sim 10^{14}$ M$_\odot$) the core itself becomes isentropic (Fig. 4, right column).

Then, we analysed the evolution of the entropy distribution by tracking gas particles to reconstruct their median Lagrangian histories and help interpret the origin of the entropy excess relative to the self-similar expectation. The results in Figs 6 and 7 suggest a picture where (AGN) feedback preferentially removes low-entropy gas from the progenitors before it can fall into the core region, replacing it with hotter and higher entropy material. This mechanism effectively erases the central entropy gradient, preventing the formation of a well-defined CC. A striking example of this effect is seen in the core region, where gas tracked in NR simulations retains a power-law entropy distribution, while its counterpart in the Ref run shows a flattened profile at late times. Notably, the halocentric distance histories (top row of Figs 6 and 7) reveal that this redistribution is not simply a matter of local heating. Gas is physically displaced, in agreement with the findings of McCarthy et al. (2011), altering the overall thermodynamic balance of the system.

We reiterate that the entropy excess seen in our simulated clusters is not unique to EAGLE-like simulation models, but is a common feature of many cosmological simulations. The entropy levels in our clusters at $z = 0$ (Fig. 4, bottom row) are consistently higher than observations of like-mass objects by Sun et al. (2009) and Pratt et al. (2010), but align with recent observational results (X-GAP objects show entropy plateaus, Eckert et al. 2024) and trends seen in other cosmological simulations such as ILLUSTRISTNG (Pillepich et al. 2018), SIMBA (Davé et al. 2019), and FABLE (Henden et al. 2018). Other X-ray observations of galaxy groups highlighted departures from power laws: ESO 3060170 (Sun et al. 2004); AWM5, which has a clear entropy plateau between 10–50 kpc similar to that of our group (phase C) in the inner region, but recovering a self-similar power law at larger radii (Baldi et al. 2009); Nest 200047, where the entropy profile is a power law, but 1 dex higher than self-similar expectations with a baryon fraction of 0.15 (Majumder et al. 2025). Recent results by Eckert et al. (2025) depicted SDSSTG 4436 as a (fossil) group with a flat inner entropy profile, and evidence of a giant AGN outburst that prevented the formation of a self-regulating feedback cycle – and therefore destroyed the CC. This scenario is remarkably similar to our group's, whose entropy levels in the IGM are found to be raised by premature feedback at early times (Section 5). On the other hand, the profiles from the group AWM4 (Gastaldello et al. 2008; O'Sullivan et al. 2010) obtained with *Chandra* present a system with high-entropy levels, but evidence of little heating.

Focusing again on the observational samples of Sun et al. (2009) and Pratt et al. (2010), our entropy levels exceed most observed values by up to an order of magnitude in group-mass haloes and remain systematically elevated by ≈ 0.4 dex in cluster cores, suggesting that AGN feedback, as implemented, is excessively efficient at heating and ejecting gas. This is evident in lower mass haloes, where the gravitational potential is weaker, allowing outflows to more easily expel low-entropy material, as also found in McCarthy et al. (2011) and Lehle et al. (2024). The redshift evolution of the baryon fraction (Fig. 3, top row) further supports this: while the cluster maintains a roughly constant baryon fraction, the group exhibits progressive baryon depletion, indicating that AGN-driven outflows are disproportionately affecting smaller systems. The corresponding increase in core entropy reflects a systematic removal of dense, low-entropy gas, leaving behind an IGM dominated by a high-entropy phase.

As commented by Bahar et al. (2024), the implementation of AGN feedback efficiencies that scale with BH accretion rate (Gaspari, Brighenti & Ruszkowski 2013) may help address this issue by reducing excess heating in groups, though it remains to be determined whether this can be achieved without causing overcooking.

Despite capturing the overall trends in gas fractions, BCG mass and star formation evolution, our simulations do not yet reproduce the observed diversity in entropy core properties, particularly the formation of long-lived CCs. Observations show that a significant fraction of clusters retain low central entropy ($K_0 \sim 10$ keV cm^2), forming well-defined CCs (Sun et al. 2009; Pratt et al. 2010). In contrast, our simulated clusters exhibit flattened entropy profiles in and around the core, characteristic of NCC objects (Fig. 4, bottom right). However, it is important to recognize that X-ray-selected samples suffer from a known CC bias, preferentially detecting low entropy, centrally concentrated systems, and potentially missing high-entropy groups (Eckert et al. 2011). On group scales, especially, this bias means the true distribution of central entropy levels may be skewed; therefore, the entropy-core problem may be overstated. Moreover, with only two haloes simulated, it is unclear a priori whether our particular systems should correspond to observed CC or NCC populations. (A larger suite of simulations is required to establish whether the entropy excess we find is a generic feature or reflects the selection of atypical objects.) Moreover, there are no detailed observational results on systems with $M_{500} \approx 9 \times 10^{12}$ M$_\odot$ yet, suggesting that future work should target simulations of objects in the range of few $\times 10^{13}$ M$_\odot$ to closely match existing observational samples.

Nevertheless, the discrepancy suggests that our AGN feedback implementation might lack the necessary complexity to control and sustain a self-regulated cooling cycle. Observed AGNs operate in episodic bursts, alternating between phases of strong heating and relative quiescence, allowing cooling flows to intermittently re-establish (McDonald et al. 2017; Rossetti et al. 2017) and potentially form stable CCs. However, the snapshots of our simulations are not sampled at a high enough frequency to resolve the variability of the cSMBH, usually around or below the kyr time-scale; future works should aim to produce this data to test the link between entropy plateaus and BH variability.

Energy injection schemes of AGN feedback are also key to self-regulation dynamics and, therefore, the core entropy levels. Recent work on isolated haloes (Huško et al. 2024) showed that purely thermal isotropic feedback, such as that used in the Ref model, increases the entropy excess in the core and hinders the formation of CCs, as do purely kinetic jets. However, adopting a hybrid kinetic-thermal scheme appears to preserve CCs by preferentially removing gas along specific directions while preventing excessive SMBH mass growth. Therefore, refining the AGN modelling and introducing a mixed thermal and jet-like anisotropic mechanisms appear to be the natural next steps, with the knowledge that varying viscosity and artificial conduction implementations in the hydrodynamics scheme can also have a similar overall impact on the IGM. However, it is possible that these changes, alone, cannot help recover power-law-like entropy profiles from an otherwise entropy plateau. Nevertheless, simulations with cosmological accretion produce strikingly different profiles than isolated objects (see Table 1), so it remains clear that new subgrid models designed to experiment on the entropy excess should be tested in a cosmological setting. Finally, adjustments to the cooling physics could also help recover power-law-like entropy profiles. For instance, the ROMULUS-C subgrid model – where metal cooling is switched off above 10^4 K – appears to preserve CCs (Tremmel et al. 2019) until merging activity destroys them following the predictions of well-known processes. However, *ad hoc* reductions of the cooling rate are to be considered unphysical.

We envisage two potential avenues to increase the diversity in simulated entropy profiles. The first is improving the modelling of multiphase cooling and condensation in the presence of magnetic fields (e.g. Grete et al. 2025), which can act as an additional channel to inject and transfer energy and influence the gas mixing (Ehlert et al. 2021). Another key improvement would be the incorporation of mechanical AGN feedback via kinetic jets, which many observed massive clusters possess. Thermal feedback alone may be too isotropic and efficient at raising entropy, while kinetic outflows, when appropriately calibrated, could preferentially remove gas along certain directions, preserving denser filaments that facilitate cooling.

The details of SMBH seeding could also play an important role. In the lower resolution BAHAMAS runs (McCarthy et al. 2017), SMBHs were seeded in 10^{11} M$_\odot$ haloes rather than 10^{10} M$_\odot$ as in our simulations, resulting in a later onset of AGN feedback. Therefore, group progenitors in BAHAMAS retain almost their full baryon load by the time they grow to $\sim 10^{12}$ M$_\odot$, curbing early low-entropy gas ejection and producing CCs with realistic gas fractions. By contrast, higher resolution EAGLE-type simulations like ours do seed SMBHs earlier and in smaller haloes, potentially ejecting gas too violently and too early, and hence flattening entropy profiles well above the NR baseline (Voit et al. 2005). Observationally, measurements of entropy profiles and hot gas fractions for systems of mass $\sim 10^{12}$ M$_\odot$ at high redshift would help discriminate SMBH-seeding strategies to adopt in numerical simulations; however, very little is still known about this class of objects.

Upcoming X-ray missions, such as *XRISM* and *Athena*, are expected to produce significantly improved constraints on entropy profiles across redshift and halo masses. A key observational test for our findings will be measuring the radial entropy gradients in CC and NCC clusters to determine whether they match the predicted entropy plateaus in simulations (e.g. Fig. 4). Additionally, the mass-limited SZ-selected cluster samples, like *Planck* and CHEX-MATE (CHEX-MATE Collaboration 2021), with new high-resolution X-ray data (e.g. *eROSITA*) will help mitigate biases inherent to existing X-ray-selected samples, improving the statistical robustness of CC fraction estimates (Andrade-Santos et al. 2017; Yuan & Han 2020). The recently introduced X-GAP sample also aims to provide an unbiased catalogue of groups observed by *XMM–Newton* with data out to r_{500}; preliminary results (Eckert et al. 2024) have shown a large entropy excess and flat entropy profiles similar to those of our group at $z = 0$ (Fig. 4), in contrast to the power-law-like ones of X-COP (Eckert et al. 2022). This systematic survey has the potential to help gain more clarity on the diversity of entropy profiles, so far emphasized only by individual observations of a few exceptional systems, like the ones discussed above.

Beyond entropy, turbulence, and bulk motion measurements from *XRISM* will help probe the role of IGM mixing. If simulations are overpredicting entropy levels due to excessive AGN heating, these observations should reveal lower turbulent energy fractions in real clusters compared to models, particularly in intermediate-mass systems ($M_{500} \sim 10^{13} - 10^{14}$ M$_\odot$). Along these lines, high-resolution simulations should explore alternative entropy transport mechanisms beyond artificial conduction, such as cosmic-ray heating (Ruszkowski, Yang & Reynolds 2017), anisotropic conduction (Yang & Reynolds 2016; Pellissier, Hahn & Ferrari 2023), and SMBH spin–jet coupling (Reynolds 2021; Huško et al. 2024), which is currently missing in the EAGLE physical models.

Additionally, radio observations (e.g. *LOw-Frequency ARray*, *Very Large Array*, and *Square Kilometer Array*) can further help

constrain AGN outflow structures and their impact on entropy redistribution, potentially hinting at new ways to model AGNs in simulations. Recently, González Villalba et al. (2025), using MAGNETICUM simulations in combination with X-ray and radio observations, showed that the CC fractions decrease systematically toward higher mass clusters, highlighting the need for refined AGN models that dynamically regulate feedback efficiency based on local gas conditions, for simulations and observations to agree.

Recent kinetic SZ (kSZ) effect measurements (Schaan et al. 2021) indicate that most simulations, except for ILLUSTRIS (Vogelsberger et al. 2014), would require significantly stronger AGN feedback to match observed galaxy clustering relations. Results from the FLAMINGO simulations suggest that their fiducial feedback model is insufficiently energetic, and stronger feedback can help match kSZ data and slightly alleviate the S_8 tension by reducing small-scale clustering amplitude (McCarthy et al. 2025). 7wever, our results from Paper I and those from FLAMINGO (see fig. 7 of Braspenning et al. 2024) have shown that stronger feedback is undesirable because it increases the core entropy and leads to entropy plateaus, exacerbating the tension with X-ray observations. At present, no feedback prescription in simulations is known to match observational results at all scales – in the field, $\gtrsim$Mpc, with kSZ and in overdense halos, $\lesssim$Mpc, with X-rays – simultaneously.

The emergence of entropy plateaus at specific halo masses is a robust, physically motivated feature of structure formation, and has now been observed in low-z groups (Eckert et al. 2024), who report large entropy excesses and flat cores similar to ours. While many observed clusters still exhibit classic CC power-law gradients, recent results of X-GAP and SDSSTG 4436 show that observations too found a diversity of entropy profiles. This underscores the need for AGN feedback models that can reproduce the full spectrum of entropy shapes. In this regard, the manifestation of entropy plateaus in individual systems non-trivially depends on the details of the heating and cooling, which must be carefully controlled and characterized. Therefore, feedback prescriptions must be refined to (i) accurately capture both plateau and power-law behaviours without undermining other key cluster properties, and (ii) remain consistent across sub- and super-Mpc scales, from kSZ to X-ray observables. The next generation of simulations, benefiting from increased resolution and updated subgrid models, will be key to further understanding these issues, examining the correlations between baryonic physics and cosmology, and helping interpret results from upcoming observational surveys.

DATA AND CODE AVAILABILITY

The SWIFT code is licensed under the GNU General Public License v3.0 and publicly available at gitlab.cosma.dur.ac.uk/swift/swiftsim. The VELOCIRAPTOR structure-finding code is publicly available at github.com/ICRAR/VELOCIraptor-STF and distributed under the MIT License. The raw snapshots and halo catalogues can be made available upon reasonable request to the corresponding author. The code used for the analysis and the data products used to generate the figures are documented and made publicly available at the following repository: github.com/edoaltamura/entropy-core-evolution.

ACKNOWLEDGEMENTS

We thank the anonymous reviewer for their comments, which improved the quality of this work. EA thanks Adrian Jenkins and Alastair Basden for high-performance computing support. This work used the DiRAC@Durham facility managed by the Institute for Computational Cosmology on behalf of the STFC DiRAC HPC Facility (www.dirac.ac.uk). The equipment was funded by BEIS capital funding via STFC capital grants ST/K00042X/1, ST/P002293/1, ST/R002371/1, and ST/S002502/1, Durham University, and STFC operations grant ST/R000832/1. DiRAC is part of the National e-Infrastructure. EA acknowledges the STFC studentship grant ST/T506291/1 and support from the Jodrell Bank Centre for Astrophysics at the University of Manchester. The research in this paper made use of the following software packages and libraries: PYTHON (Van Rossum & Drake 1995), NUMPY (Harris et al. 2020), SCIPY (Virtanen et al. 2020), NUMBA (Lam, Pitrou & Seibert 2015), MATPLOTLIB (Hunter 2007; Caswell et al. 2021), SWIFTSIMIO (Borrow & Borrisov 2020), ASTROPY (Robitaille et al. 2013; Price-Whelan et al. 2022), UNYT (Goldbaum et al. 2018), SWIFT version 0.9.0 (Schaller et al. 2018, 2024), and VELOCIRAPTOR (Elahi et al. 2019).

REFERENCES

Akino D. et al., 2022, PASJ, 74, 175
Altamura E., 2023, PhD thesis, The University of Manchester, UK
Altamura E., Kay S. T., Bower R. G., Schaller M., Bahé Y. M., Schaye J., Borrow J., Towler I., 2023, MNRAS, 520, 3164
Andrade-Santos F. et al., 2017, ApJ, 843, 76
Bahar Y. E. et al., 2024, A&A, 691, A188
Bahé Y. M. et al., 2022, MNRAS, 516, 167
Baldi A., Forman W., Jones C., Nulsen P., David L., Kraft R., Simionescu A., 2009, ApJ, 694, 479
Barai P., Murante G., Borgani S., Gaspari M., Granato G. L., Monaco P., Ragone-Figueroa C., 2016, MNRAS, 461, 1548
Barnes D. J. et al., 2018, MNRAS, 481, 1809
Barnes D. J., Kay S. T., Henson M. A., McCarthy I. G., Schaye J., Jenkins A., 2017a, MNRAS, 465, 213
Barnes D. J. et al., 2017b, MNRAS, 471, 1088
Benisty D., Vasiliev E., Evans N. W., Davis A.-C., Hartl O. V., Strigari L. E., 2022, ApJ, 928, L5
Beraldo e Silva L., Mamon G. A., Duarte M., Wojtak R., Peirani S., Boué G., 2015, MNRAS, 452, 944
Bluck A. F. L. et al., 2024, ApJ, 961, 163
Bluck A. F. L., Piotrowska J. M., Maiolino R., 2023, ApJ, 944, 108
Bondi H., Hoyle F., 1944, MNRAS, 104, 273
Booth C. M., Schaye J., 2009, MNRAS, 398, 53
Borgani S., Kravtsov A., 2011, Adv. Sci. Lett., 4, 204
Borrow J., Borrisov A., 2020, J. Open Source Softw., 5, 2430
Borrow J., Schaller M., Bahé Y. M., Schaye J., Ludlow A. D., Ploeckinger S., Nobels F. S. J., Altamura E., 2023, MNRAS, 526, 2441
Borrow J., Schaller M., Bower R. G., Schaye J., 2022, MNRAS, 511, 2367
Bourne M. A., Sijacki D., 2021, MNRAS, 506, 488
Bower R. G., 1997, MNRAS, 288, 355
Bower R. G., Schaye J., Frenk C. S., Theuns T., Schaller M., Crain R. A., McAlpine S., 2017, MNRAS, 465, 32
Braspenning J. et al., 2024, MNRAS, 533, 2656
Bryan G. L., 2000, ApJ, 544, L1
Caswell T. A. et al., 2021, matplotlib/matplotlib: REL: v3.4.2 (v3.4.2) . Zenodo. Avalable at: https://doi.org/10.5281/zenodo.4743323
Chabrier G., 2003, PASP, 115, 763
Chadayammuri U., Tremmel M., Nagai D., Babul A., Quinn T., 2021, MNRAS, 504, 3922
CHEX-MATE Collaboration, 2021, A&A, 650, A104
Clerc N. et al., 2024, A&A, 687, A238
Crain R. A. et al., 2015, MNRAS, 450, 1937
Dalla Vecchia C., Schaye J., 2012, MNRAS, 426, 140
Davé R., Anglés-Alcázar D., Narayanan D., Li Q., Rafieferantsoa M. H., Appleby S., 2019, MNRAS, 486, 2827
Dekel A., Mandelker N., 2014, MNRAS, 444, 2071
Diemer B., 2022, MNRAS, 513, 573

Dolag K., Gaensler B. M., Beck A. M., Beck M. C., 2015, MNRAS, 451, 4277
Donahue M., Voit G. M., 2022, Phys. Rep., 973, 1
Eckert D. et al., 2025, preprint (arXiv:2506.13907)
Eckert D., Ettori S., Pointecouteau E., van der Burg R. F. J., Loubser S. I., 2022, A&A, 662, A123
Eckert D., Gastaldello F., O'Sullivan E., Finoguenov A., Brienza M., X-GAP Collaboration, 2024, Galaxies, 12, 24
Eckert D., Molendi S., Paltani S., 2011, A&A, 526, A79
Eddington A. S., 1926, The Internal Constitution of the Stars. Cambridge Univ. Press, Cambridge
Ehlert K., Weinberger R., Pfrommer C., Springel V., 2021, MNRAS, 503, 1327
Elahi P. J., Cañas R., Poulton R. J. J., Tobar R. J., Willis J. S., Lagos C. d. P., Power C., Robotham A. S. G., 2019, Publ. Astron. Soc. Aust., 36, e021
Faltenbacher A., Hoffman Y., Gottlöber S., Yepes G., 2007, MNRAS, 376, 1327
Faucher-Giguère C.-A., 2020, MNRAS, 493, 1614
Gaspari M., Brighenti F., D'Ercole A., Melioli C., 2011, MNRAS, 415, 1549
Gaspari M., Brighenti F., Ruszkowski M., 2013, Astron. Nachr., 334, 394
Gaspari M., Brighenti F., Temi P., Ettori S., 2014, ApJ, 783, L10
Gastaldello F., Buote D. A., Brighenti F., Mathews W. G., 2008, ApJ, 673, L17
Genel S., Vogelsberger M., Nelson D., Sijacki D., Springel V., Hernquist L., 2013, MNRAS, 435, 1426
Goldbaum N. J., ZuHone J. A., Turk M. J., Kowalik K., Rosen A. L., 2018, J. Open Source Softw., 28, 809
González Villalba J. A., Dolag K., Biffi V., 2025, A&A, 694, A232
Grete P., O'Shea B. W., Glines F. W., Prasad D., Wibking B. D., Fournier M., Brüggen M., Voit M., 2025, preprint (arXiv:2502.13213)
Hansen S. H., Sparre M., 2012, ApJ, 756, 100
Harris C. R. et al., 2020, Nature, 585, 357
He P., Kang D.-B., 2010, MNRAS, 406, 2678
Henden N. A., Puchwein E., Shen S., Sijacki D., 2018, MNRAS, 479, 5385
Henriksen R. N., 2009, ApJ, 690, 102
Hopkins P. F., Hernquist L., 2009, ApJ, 698, 1550
Hoyle F., Lyttleton R. A., 1939, Proc. Camb. Phil. Soc., 35, 405
Hunter J. D., 2007, Comput. Sci. Eng., 9, 90
Huško F., Lacey C. G., Schaye J., Nobels F. S. J., Schaller M., 2024, MNRAS, 527, 5988
Huško F., Lacey C. G., Schaye J., Schaller M., Nobels F. S. J., 2022, MNRAS, 516, 3750
Jenkins A., 2010, MNRAS, 403, 1859
Jenkins A., 2013, MNRAS, 434, 2094
Kandrup H. E., Vass I. M., Sideris I. V., 2003, MNRAS, 341, 927
Katz N., White S. D. M., 1993, ApJ, 412, 455
Kay S. T., da Silva A. C., Aghanim N., Blanchard A., Liddle A. R., Puget J.-L., Sadat R., Thomas P. A., 2007, MNRAS, 377, 317
Kennicutt R. C., Jr, 1998, ApJ, 498, 541
Knight P. A., Ponman T. J., 1997, MNRAS, 289, 955
Kulier A., Ostriker J. P., Natarajan P., Lackner C. N., Cen R., 2015, ApJ, 799, 178
Lam S. K., Pitrou A., Seibert S., 2015, Proc. Second Workshop on the LLVM Compiler Infrastructure in HPC, Numba: A LLVM-based Python JIT Compiler. Association for Computing Machinery, Austin, Texas, p. 1
Le Brun A. M. C., McCarthy I. G., Schaye J., Ponman T. J., 2014, MNRAS, 441, 1270
Lebovitz N. R., 1965, ApJ, 142, 229
Lehle K., Nelson D., Pillepich A., Truong N., Rohr E., 2024, A&A, 687, A129
Lin H. W., McDonald M., Benson B., Miller E., 2015, ApJ, 802, 34
Maiolino R. et al., 2012, MNRAS, 425, L66
Majumder A. et al., 2025, preprint (arXiv:2506.11312)
McCarthy I. G. et al., 2010, MNRAS, 406, 822
McCarthy I. G. et al., 2025, MNRAS, 540, 143
McCarthy I. G., Schaye J., Bird S., Le Brun A. M. C., 2017, MNRAS, 465, 2936
McCarthy I. G., Schaye J., Bower R. G., Ponman T. J., Booth C. M., Dalla Vecchia C., Springel V., 2011, MNRAS, 412, 1965
McDonald M. et al., 2017, ApJ, 843, 28
Mirakhor M. S., Walker S. A., 2020, MNRAS, 497, 3204
Navarro J. F., Frenk C. S., White S. D. M., 1997, ApJ, 490, 493
Nelson D. et al., 2019, MNRAS, 490, 3234
Nelson D., Pillepich A., Ayromlou M., Lee W., Lehle K., Rohr E., Truong N., 2024, A&A, 686, A157
Nobels F. S. J., Schaye J., Schaller M., Bahé Y. M., Chaikin E., 2022, MNRAS, 515, 4838
O'Sullivan E., Giacintucci S., David L. P., Vrtilek J. M., Raychaudhury S., 2010, MNRAS, 407, 321
Oppenheimer B. D., Babul A., Bahé Y., Butsky I. S., McCarthy I. G., 2021, Universe, 7, 209
Pellissier A., Hahn O., Ferrari C., 2023, MNRAS, 522, 721
Pillepich A. et al., 2018, MNRAS, 473, 4077
Piotrowska J. M., Bluck A. F. L., Maiolino R., Peng Y., 2022, MNRAS, 512, 1052
Planck Collaboration VI, 2020, A&A, 641, A6
Plastino A. R., Plastino A., 1993, Phys. Lett. A, 174, 384
Ploeckinger S., Schaye J., 2020, MNRAS, 497, 4857
Poon H., Okabe N., Fukazawa Y., Akino D., Yang C., 2023, MNRAS, 520, 6001
Popesso P. et al., 2024, preprint (arXiv:2411.16555)
Pratt G. W. et al., 2010, A&A, 511, A85
Price-Whelan A. M. et al., 2022, ApJ, 935, 167
Reynolds C. S., 2021, ARA&A, 59, 117
Richings J., Frenk C., Jenkins A., Robertson A., Schaller M., 2021, MNRAS, 501, 4657
Robitaille T. P. et al., 2013, A&A, 558, A33
Rosas-Guevara Y. M. et al., 2015, MNRAS, 454, 1038
Rossetti M., Gastaldello F., Eckert D., Della Torre M., Pantiri G., Cazzoletti P., Molendi S., 2017, MNRAS, 468, 1917
Ruppin F., McDonald M., Bleem L. E., Allen S. W., Benson B. A., Calzadilla M., Khullar G., Floyd B., 2021, ApJ, 918, 43
Ruszkowski M., Yang H. Y. K., Reynolds C. S., 2017, ApJ, 844, 13
Savitzky A., Golay M. J., 1964, Anal. Chem., 36, 1627
Schaan E. et al., 2021, Phys. Rev. D, 103, 063513
Schaller M. et al., 2024, MNRAS, 530, 2378
Schaller M., Gonnet P., Draper P. W., Chalk A. B. G., Bower R. G., Willis J., Hausammann L., 2018, Astrophysics Source Code Library, record ascl:1805.020
Schaye J. et al., 2010, MNRAS, 402, 1536
Schaye J. et al., 2015, MNRAS, 446, 521
Schaye J. et al., 2023, MNRAS, 526, 4978
Schaye J., 2004, ApJ, 609, 667
Schaye J., Dalla Vecchia C., 2008, MNRAS, 383, 1210
Schmidt M., 1959, ApJ, 129, 243
Schwarzschild M., 1958, Structure and Evolution of the Stars. Princeton Univ. Press, Princeton, NJ
Shakura N. I., Sunyaev R. A., 1973, A&A, 24, 337
Simionescu A., Werner N., Mantz A., Allen S. W., Urban O., 2017, MNRAS, 469, 1476
Sun M., Forman W., Vikhlinin A., Hornstrup A., Jones C., Murray S. S., 2004, ApJ, 612, 805
Sun M., Voit G. M., Donahue M., Jones C., Forman W., Vikhlinin A., 2009, ApJ, 693, 1142
Tacchella S. et al., 2019, MNRAS, 487, 5416
Thorne K. S., 1966, ApJ, 144, 201
Tormen G., Bouchet F. R., White S. D. M., 1997, MNRAS, 286, 865
Tozzi P., Norman C., 2001, ApJ, 546, 63
Tremmel M. et al., 2019, MNRAS, 483, 3336
Tremmel M., Karcher M., Governato F., Volonteri M., Quinn T. R., Pontzen A., Anderson L., Bellovary J., 2017, MNRAS, 470, 1121
Van Rossum G., Drake F. L., Jr, 1995, Python Tutorial, Vol. 620. Centrum voor Wiskunde en Informatica Amsterdam, The Netherlands
Vazza F., 2011, MNRAS, 410, 461

Vikhlinin A., Kravtsov A., Forman W., Jones C., Markevitch M., Murray S. S., Van Speybroeck L., 2006, ApJ, 640, 691
Virtanen P. et al., 2020, Nat. Methods, 17, 261
Vogelsberger M. et al., 2014, MNRAS, 444, 1518
Voit G. M., Bryan G. L., 2001, Nature, 414, 425
Voit G. M., Bryan G. L., Balogh M. L., Bower R. G., 2002, ApJ, 576, 601
Voit G. M., Kay S. T., Bryan G. L., 2005, MNRAS, 364, 909
Walker S. A., Fabian A. C., Sanders J. S., George M. R., 2012, MNRAS, 427, L45
Wendland H., 1995, Adv. Comput. Math., 4, 389
Wiersma R. P. C., Schaye J., Theuns T., Dalla Vecchia C., Tornatore L., 2009, MNRAS, 399, 574
Yang H. Y. K., Reynolds C. S., 2016, ApJ, 818, 181
Yuan Z. S., Han J. L., 2020, MNRAS, 497, 5485

APPENDIX: ENTROPY DISTRIBUTION IN THE NR RUNS

In addition to the results in Section 4.4, we show the scaled entropy profiles for the group and cluster run with the NR configuration, i.e. only gravity and hydrodynamics, in Fig. A1. The layout is the same as in the Ref profiles: three colours correspond to three evolutionary phases (indicated at the top of the panels), and the hues correspond to runs with different particle-mass resolutions. The NR profiles of both objects are power-law-like down to the core radius in phases A and B, in line with predictions from Voit et al. (2005), shown in green.

While the NR group maintains a CC to $z = 0$, the cluster's central entropy level departs from the self-similar power law. Given the NR model specifications, the flattening of the cluster's profile can be associated with artificial conduction, which is known to result in the mixing of low- and high-entropy gas. Despite this effect, we note that the entropy level for the cluster profile at the core is $\approx 0.2\,K_{500}$, which is half of that obtained with Ref; moreover, the NR isentropic core extends to $\approx 0.25\,r_{500}$, while the Ref NCCs are more extended in size ($\approx 0.5\,r_{500}$).

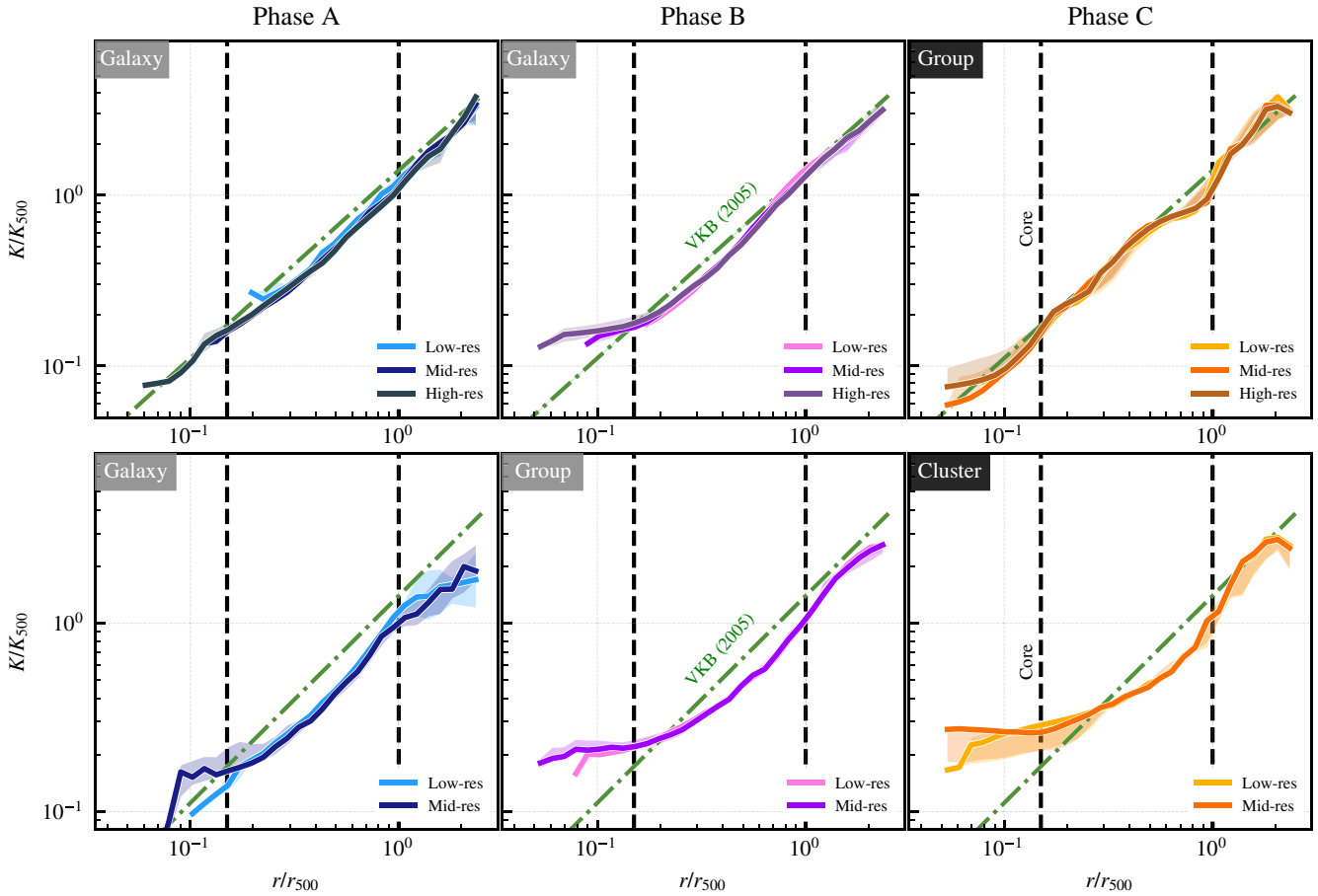

Figure A1. Scaled entropy profiles as in Fig. 4, but for the NR model.

This paper has been typeset from a TEX/LATEX file prepared by the author.